LRP 428/91 June 1991

Papers contributed to the
18th EPS CONFERENCE ON CONTROLLED
FUSION AND PLASMA PHYSICS

Berlin, Germany, June 1991

MEASUREMENT OF TOROIDAL AND POLOIDAL PLASMA ROTATION IN TCA

B. P. Duval, B. Joye, B. Marchal

Centre de Recherches en Physique des Plasmas
Association Euratom-Confédération Suisse
Ecole Polytechnique Fédérale de Lausanne
CH-1015 Lausanne, Switzerland

Introduction

The stimulus for measuring the toroidal and poloidal rotation velocities on TCA (R=0.615m, a=0.18m, Ip=130kA), was the large density rise observed with high power Alfvén Wave Heating (AWH) [1]. From the measured velocities, we can deduce the radial electric field in the plasma, a change in which could be responsible for the density rise. Quartz fibres with quartz windows allowed observations of the CV (227nm) and CIII (230nm) spectral lines in second order which are strong in TCA, and are emitted from r=~2a/3 and in the plasma edge respectively. A 1m Czerny-Turner visible spectrometer with a multichannel OMA detector equipped with a 2400l/mm grating recorded a spectral line profile every 2ms through the 200ms discharge. On TCA, these spectral features are completely unpolluted by other spectral lines which simplifies data analysis and improves the data quality. For the toroidal measurements, opposing tangential windows permitted measurements with and against the plasma current, and a long slot window on top of TCA permitted poloidal measurements along near vertical chords on both the low and high field side of the plasma. When access via a quartz window was impossible, helium was injected into the discharge and the HeII (468nm) spectral line was observed in first order.

Results

Fig 1 shows the evolution of the CV toroidal plasma velocity through a discharge with a large density rise (hard puff), together with the position of the spectral feature on the OMA and its HWHM both in pixels (1pix=25μm).

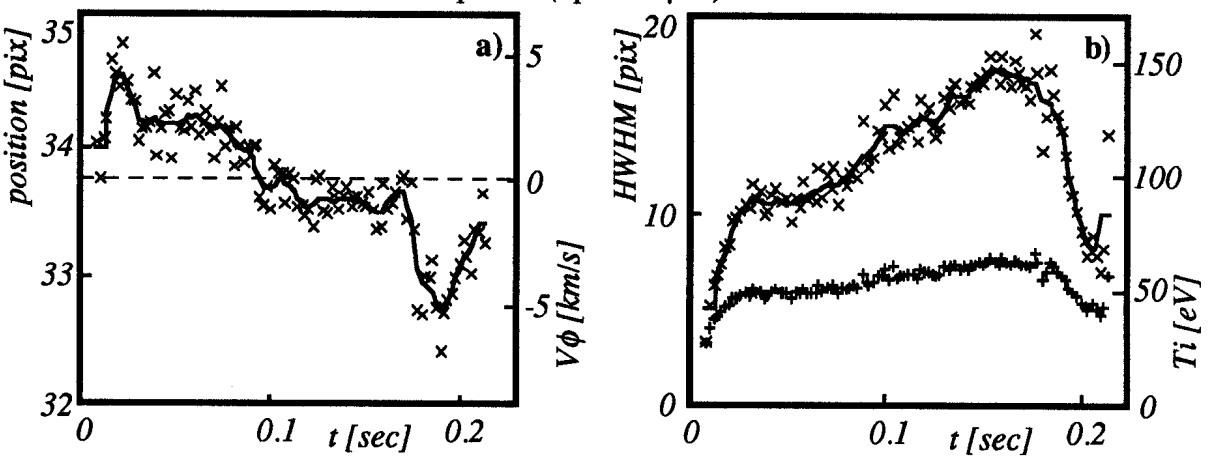

Fig I Evolution of the (a) toroidal rotation and (b) ion temperature through a discharge

To determine the absolute velocity, toroidally the plasma was viewed in and against the plasma current direction and for poloidal measurements the plasma centre was viewed to define the zero velocity reference. The spectrometer was also regularly calibrated against a spectral lamp and a correction applied based on the spectrometer temperature, measured by an array of thermistors. The measured scatter from observing a spectral lamp during a plasma discharge was ~0.5km/s. The scatter of ~1.5km/s in the CV data shown in Fig 1 is mostly due to larger Doppler broadening of the plasma spectral line. The crosses show the fitted position of each 2ms integration and the solid line is a weighted smooth across three points which has an estimated statistical error of ~0.5km/s. The deduced ion temperature has been corrected for the instrumental function. Comparing this with a peak value measured by neutral particle analysis of ~330ev the emission region is ~2a/3.

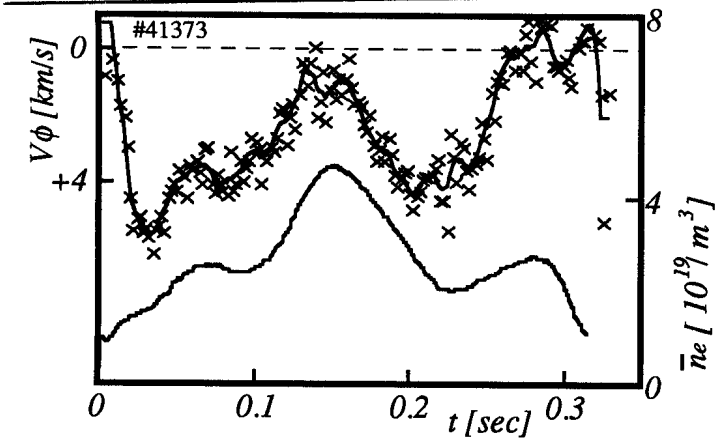

Fig 2 The evolution of the toroidal rotation velocity, in the direction of plasma current, together with the plasma density through a discharge. The rotation velocity ceases to follow the plasma density at the end of the discharge when the plasma current starts to fall.

Before we approached the effects of AWH we studied rotation with normal and hard gas puffs in which higher final densities can be achieved without plasma disruption. Fig 2 shows the evolution of the toroidal rotation of HeII and the plasma density.

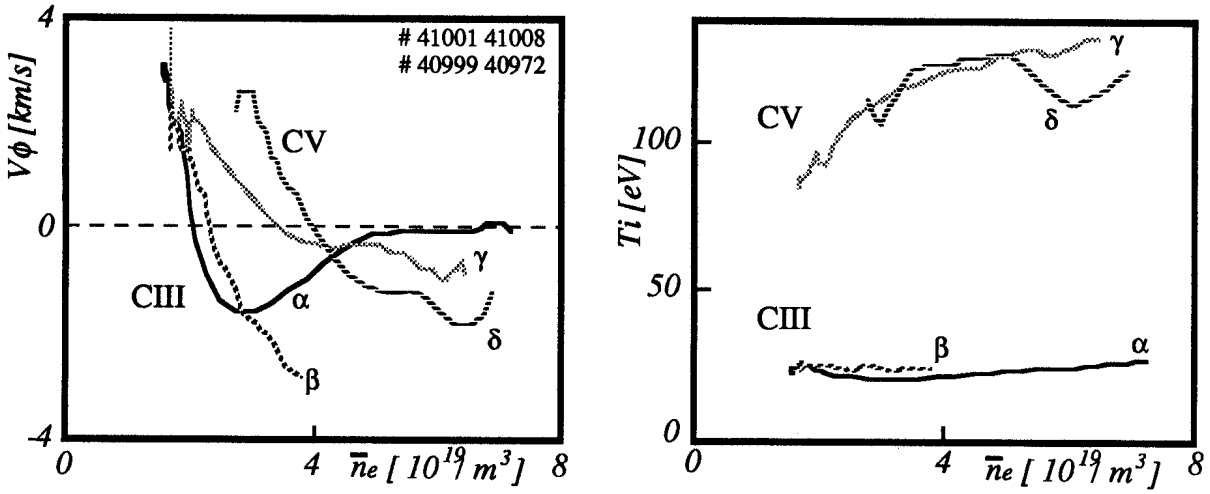

Fig 3. Traces of toroidal rotation for CIII and CV, for discharges with a lower density ramp (β and δ) and over double the same ramp rate (α and γ). where the velocity locus saturates and tends to zero. This effect is more pronounced at the plasma edge (CIII). The ion temperatures show that the discharges are otherwise similar.

The toroidal rotation closely follows the plasma density. In discharges where the density reaches a plateau, the toroidal velocity also stabilises. This dependence is less direct when a hard gas puff is used.

Fig 3 plots the measured toroidal velocity against average plasma electron density for CV and CIII for discharges with different density ramps. For the plasma edge (CIII), two discharges with different ramp rates are shown. For the higher ramp rate, the toroidal velocity ceases to rise and returns to zero. For CV, the same effect is present, although we note, as in all the velocity measurements, that the CV velocity reacts less and more slowly to gas puffing than at the edge. The temperatures are similar in both cases and it is clearly the ramp rate, and not the value of the density, that is the cause.

Fig 4 shows the poloidal velocity measurements with AWH and a hard gas puff. Positive velocities correspond to the electron diamagnetic drift direction. To demonstrate the shot to shot differences, two discharges with AWH are shown together with a hard gas puff, where the range of other observations is indicated by the shaded region. There is no clear difference which distinguishes the AWH traces, and the width of the shaded region is dominated by changes in the density ramp, and the cooling effect of the stronger gas puffs, rather than AWH effects.

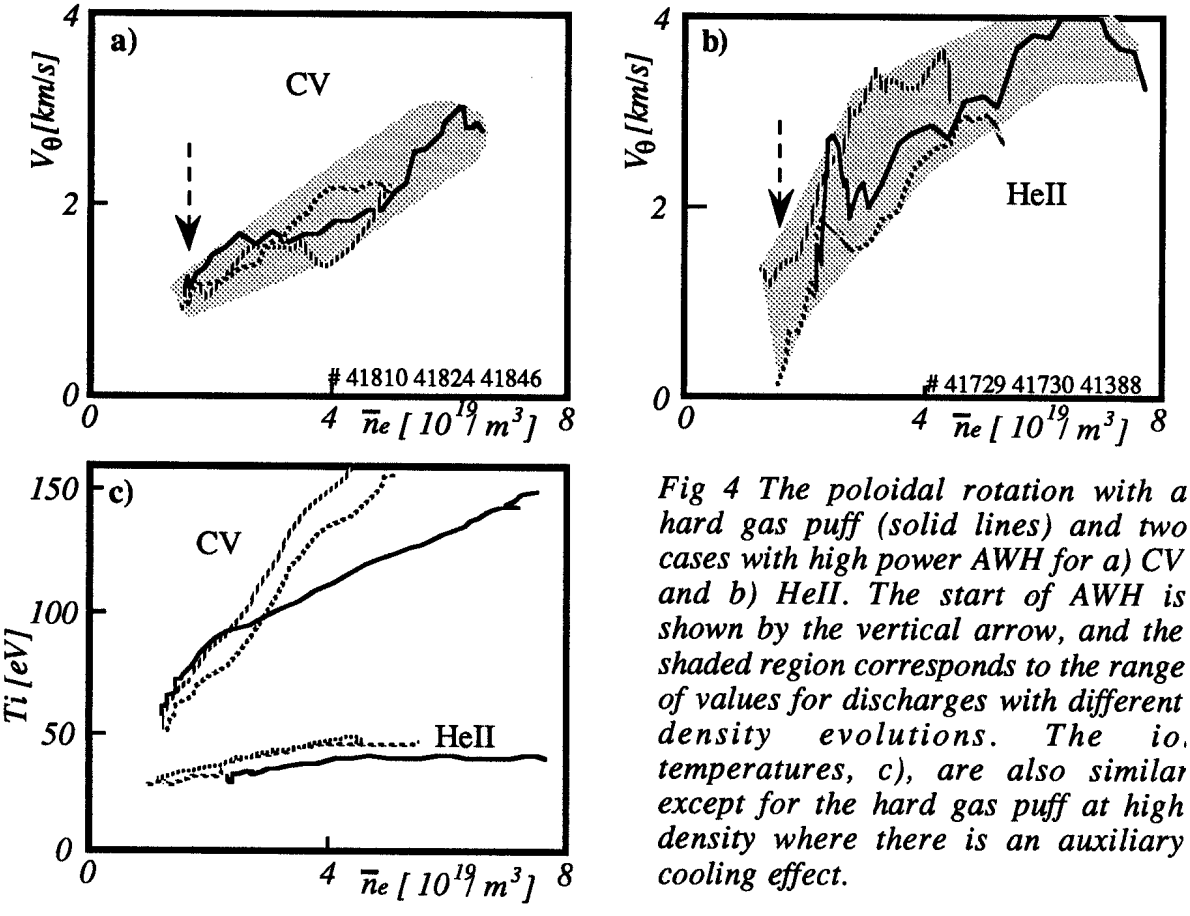

Fig 4 The poloidal rotation with a hard gas puff (solid lines) and two cases with high power AWH for a) CV and b) HeII. The start of AWH is shown by the vertical arrow, and the shaded region corresponds to the range of values for discharges with different density evolutions. The io, temperatures, c), are also similar except for the hard gas puff at high density where there is an auxiliary cooling effect.

Discussion

The radial electric field may be deduced from the force balance equation on an ion:

$$E_r - \frac{\nabla_r P_i}{n_i Z_i e} = v_\phi B_\theta - v_\theta B_\Phi$$

The contribution from the gradient is estimated to be less than 10% in all our observations, and much less in the plasma edge. Operation time restrictions precluded a measurement of toroidal velocity with high power AWH, but since its contribution to the deduced electric field is ~10%, the error introduced is small. With AWH, no significant increase in the poloidal velocity, and thus radial electric field, was measured that could explain the large associated density rise. Good agreement between the values measured from HeII and CIII (-1kV/m at low density rising to -6kV/m) was observed. The value deduced from CV was the same at low density and ~1.5x lower at high density. This is considerably lower than that observed on DIIID [2] which is a larger machine.

Conclusion

With optimal observation geometry we have measured both the toroidal and poloidal rotation velocities in the edge and in the bulk of the TCA plasma. Regular calibration and correction for variations in the spectrometer temperature permitted a measurement with an error of ~0.5km/s which is an order of magnitude smaller than the range of measured velocities.

In general, changes in the velocities are observed to be stronger and faster in the plasma edge than in the plasma bulk. With increasing density, the toroidal velocity is observed to change sign and follow the plasma density, while the poloidal velocity increases. These two effects lead to an increase in the absolute value of the radial electric field. With very strong gas puffing, the toroidal velocity is observed to again reverse and tend to zero, an effect which is stronger as the gradient of the density ramp is increased. Comparison between gas puffing and high power AWH does not show a significant difference in the radial electric field that could be responsible for the large associated density rise, which still remains unexplained.

Acknowledgments

We wish to thank the whole TCA team for the technical support. This work was partially supported by Le Fonds National Suisse de la Recherche Scientifique.

References

[1] G.A. Collins et al., Proc. of the 12th European Conference on Control Fusion and Plasma Physics, Budapest, Vol 9 p248 (1985).

[2] R.J. Groebner, K.H. Burrell, R.P. Seraydarian, *"Role of Edge Electric Field and Poloidal Rotation in the L-H Transition"*, Phys. Rev. Lett., Vol 64, No 25 (1989), 3015-3018.

PELLET ABLATION STUDIES IN THE TCA TOKAMAK

M. Drakakis *, M. Dutch, B. P. Duval, Ch. Hollenstein, B. Joye,
J. B. Lister, Y. Martin, Ch. Nieswand, P. J. Paris

Centre de Recherche en Physique des Plasmas
Association Confédération Suisse - Euratom
Ecole Polytechnique Fédérale de Lausanne
21, av. des Bains
CH - 1007 Lausanne

*Present Address: University of Crete, Heraklion.

ABSTRACT *Pellets with a variation in size of an order of magnitude and of injection velocity of a factor of 4 were injected into a Tokamak with a range of plasma current and density. The penetration into the plasma has been measured against these parameters. Contrary to most ablation models, only weak scaling was found which suggests that the pellet ablation process is dominated by other factors.*

Introduction

The injector installed on TCA (R = 0.615 m, a = 0.18 m) was used to inject frozen hydrogen pellets with a large range of velocities (200 - 800 m/s) and a wide range of size (3×10^{18} - 3×10^{19} particles), into a wide variety of target plasmas. One of the main goals of this flexible system was to study pellet penetration as a function of the parameters which most frequently appear in scaling laws. Thus, in this paper, we concentrate on the pellet ablation process, rather than the effect on the plasma. Although a wide range of visible diagnostics were used to monitor the injected pellet, the Hydrogen Balmer-alpha (Hα) emission monitored with a diffused fast photomultiplier acquisition is used to define the pellet penetration. The pellet velocity was measured before and during the ablation process and used to transform the ablation time into distance.

Experiment

Several experimental runs were performed in which the pellet size and velocity together with the deuterium target plasma density and plasma current were varied over as wide a range as possible. Most of the theoretical models of pellet ablation can be summed up by a generic scaling law:

$$\text{Penetration length} \approx \frac{m_p^{\alpha}\, v_p^{\beta}}{I_p^{\gamma}\, n_e^{\delta}}$$

where m_p is the total number of particles contained in the pellet, v_p is the pellet velocity, I_p is the plasma current and n_e is the central density.

In order to extract the dependence of pellet ablation on individual parameters in Fig 1 we selected discharges in which only one of these parameters changes significantly. Apart from the dependence on the plasma current, there is surprisingly little variation in the penetration depth.

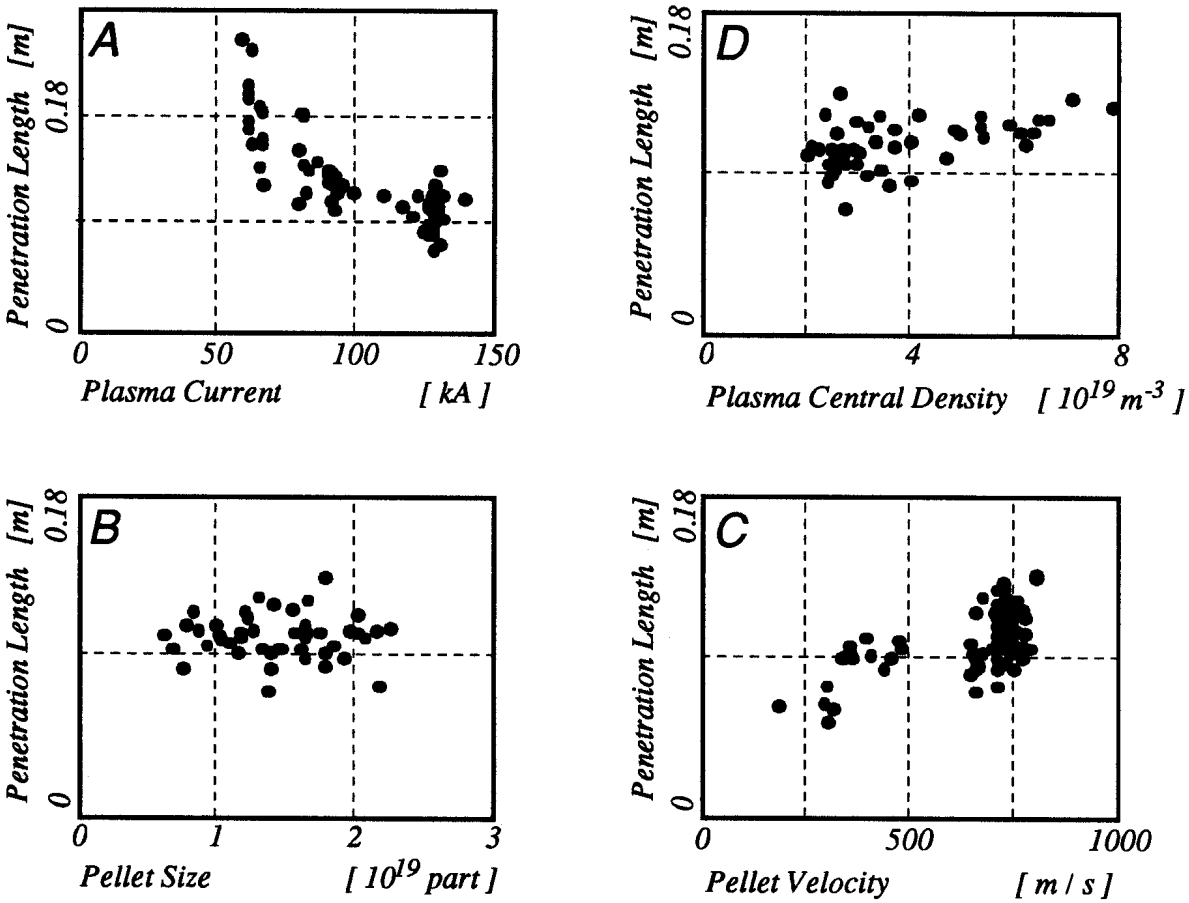

Figure 1: Pellet penetration length as a function of: A. Plasma current; B: Pellet size; C: Pellet velocity; D. Plasma central density.

The plasma current must be reduced to ~60 kA (q(a)~5-6) for the pellet to penetrate to the plasma centre. At full current (~130 kA; q(a)~3) most pellets were ablated at or before half the minor radius. Although we have plotted only the greatest penetration achieved by a pellet, the Hα line intensity was often highly peaked near a/2 indicating a localised region of high ablation. At 60 kA, where we have deep pellet penetration, the Hα line intensity shows a peak followed by a low intensity region before the machine axis. Pellets that passed the plasma centre were observed to continue with a far reduced ablation rate, suggesting that this region of the plasma was already cold.

The pellet size is seen to have little effect on the penetration (Fig 1c), and there is only a small tendency to increasing pellet penetration with increasing pellet velocity (Fig 1d). Extrapolating this dependence, a pellet velocity of ~1500 m/s would be required to reach the plasma centre. However, the validity of this simple extrapolation is cast into doubt by the presence of several nonlinear and highly localised enhanced ablation phenomena which were often observed during pellet ablation and seemed to increase in magnitude with increasing pellet velocity .

We would expect the penetration to decrease with increasing target density, although Fig 1b shows if anything the opposite dependence. Fig 2 highlights this

conclusion, where the normalised Hα line intensity is shown for two pellets of similar mass (~1.5×10^{19} pcles) and speed (~720 m/s) injected into two different target plasma densities. If the light intensity is assumed to be proportional to the local ablation rate, injection into lower target density (Fig 2a) shows a monotonic ablation rate, whereas injection into a higher target density (Fig 2b), shows a series of localised features which we term "positive striations". There was little difference between the profiles as measured by a 4 channel FIR interferometer, which leads us to conclude that the density gradient may determine the existence of striations. Fig 3 shows the number of these striations plotted against the central target plasma density where a striation is defined as a maxima which exceeding a certain threshold between two minima. The number of striations increases with the plasma density and the intensity of these striations also increases, reaching 70 % of the maximum intensity at high density. Comparison of shots with the same, and different, plasma currents did not yield a direct dependence of the location to the rational magnetic surfaces.

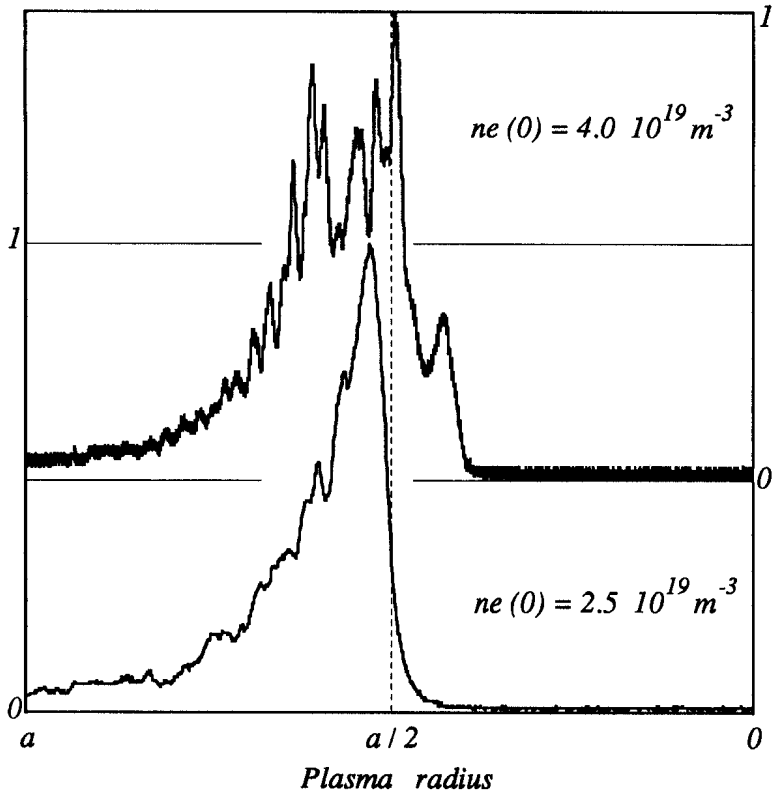

Figure 2: Normalised Hα emission intensity for two similar pellets injected into plasma with different densities.

Discussion

The above description becomes less simple as we look at the additional experimental data. We have observed different penetration distances under similar conditions, which cannot be accounted for by errors or uncertainties in the measurements.

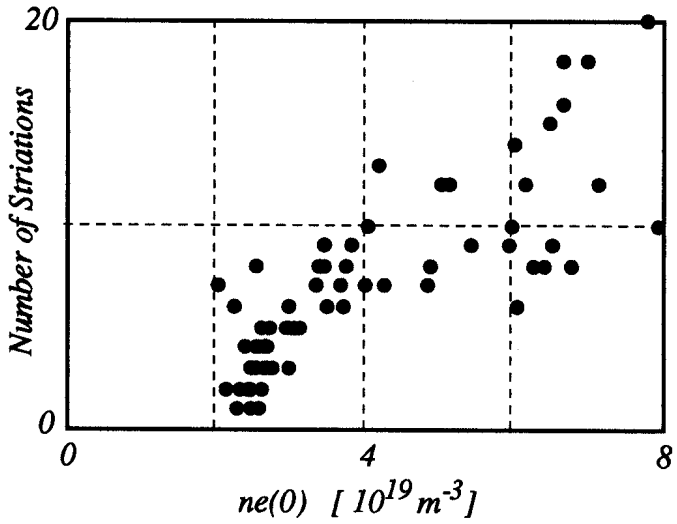

Figure 3: The number of striations is seen to increase with central plasma density, a complexity not accounted for in theoretical models of pellet ablation.

Some additional phenomena such as the increased pellet ablation in discharges with a high runaway electron content are qualitatively easy to understand. Other phenomena including curved pellet trajectories and increased penetration in the plasma current descent are not easy to quantify in the above terms. Specifically, the intensity and number of positive striations which accompany the pellet ablation have a strong influence on the penetration. These phenomena can be so strong that a pellet changes trajectory at a very localised radial position, which is often accompanied by plasma current disruption. The analysis of these effects will be greatly aided by the other available diagnostics which give complementary information on the spatial and temporal evolution of the pellet trajectory in the plasma. These additional diagnostics may help to resolve existing discrepancies between a simplistic ablation model and the complex physical processes that actually occur during the pellet penetration.

Conclusion

A large range of conditions for pellet ablation have been studied in TCA and we have investigated the experimental scaling of pellet penetration with plasma current, plasma density, pellet size and pellet velocity. We have found no dominant term in this scaling, although we did observe reduced penetration with increasing plasma current and, rather surprisingly, slightly increased penetration with increasing target plasma density. The pellet size was not found to significantly influence the penetration and there was only a slight increase in penetration with increasing pellet velocity. Other very non-linear phenomena such as positive striations and regions of reduced ablation near the plasma core appear to have a greater influence on the penetration, and these in turn appear to depend on parameters like the plasma density gradient. In general, we conclude that there is no simple formula that can guarantee a given penetration for certain conditions and that seemingly similar discharges can display quite different behaviour.

Acknowledgements

We wish to thank the whole TCA team for its excellent support. This work was partially supported by the Fonds National Suisse de la Recherche Scientifique.

EFFECTIVENESS OF X- AND O-MODE ECRH BREAKDOWN AND STARTUP IN TCA

A. Pochelon, D. R. Whaley, T. P. Goodman, B. P. Duval, M. Q. Tran, R. Behn, G. Besson, A. Cardinali†, B. Joye, A. J. Knight

Centre de Recherches en Physique des Plasmas
Association Euratom - Confédération Suisse
Ecole Polytechnique Fédérale de Lausanne
21, Av. des Bains, CH-1007 Lausanne, Switzerland
†ENEA, Frascati, I-00044 Frascati, Italy

Introduction

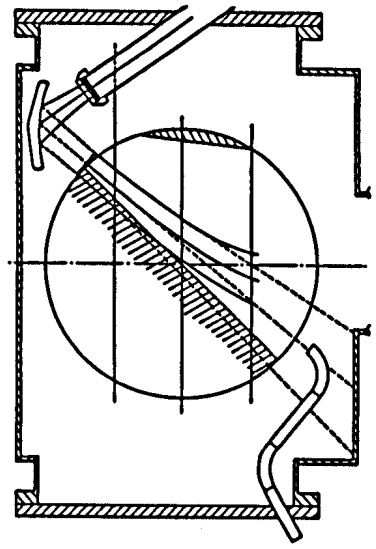

Fig. 1. Poloidal cross section of TCA.

Comparative studies of X- and O-mode launch for ECH-assisted, low loop voltage startup have been performed on the TCA tokamak. The *39GHz* TE_{02} cylindrical cavity gyrotron and microwave line, presently used on TCA[1], are planned for daily ECH startup in the upcoming TCV continuous vessel tokamak. To investigate the respective merits of X- and O-mode launch, high field side (HFS) linearly polarised HE_{11} injection has been chosen, with a steering mirror movable poloidally and toroidally ($\pm 25^\circ$ to the radial), shown in Fig. 1. In TCA (R/a = $.615m/.18m$, $B\varphi \leq 1.6T$), the ω_{ce} resonance position can be varied between $-0.5 \leq x=r/a \leq 0.5$, limited by an ω_{ce} resonance on the window for low B_φ and the maximum B_φ available for TCA. Other parameters are varied in the following ranges: $P_{ECH} < 125kW$; $10ms < \Delta t_{ECH} < 80ms$; $0.6V < V_L < 2.1V$.

Absorption characteristics in startup plasmas

As a specific microwave absorption diagnostic, two receiving horns placed opposite the steering mirror in the same poloidal plane, measure microwave transmission in both X- and O-mode polarisations. The line-integrated H_α emission is recorded by a 128-pixel camera[2], temporally resolving horizontal spatial power deposition structures. A 10-channel horizontal camera measuring visible Bremsstrahlung radiation complements the vertical H_α camera. A four-channel interferometer measures horizontal electron density profiles.

The average electron density in breakdown plasmas is typically $n_e=0.2\cdot10^{19}m^{-3}$. Hot plasma code calculations predict much higher X-mode, first-pass absorption at these low startup densities. Experimentally, X-mode launch is characterised by high first-pass absorption with a prompt density rise. Transmission measurements indicate near *100%* first-pass X-mode absorption for all startup conditions. First-pass O-mode absorption, however, is much lower and can vary from *50%* at high ECH power to near zero at low ECH power. This leads to wall reflections and mode mixing for O-mode launch.

Horizontal H_α camera profiles for X- and O-mode startup are shown in Figs. 2. For O-mode launch a narrow emission peak is seen at the ω_{ce} resonance, which is virtually

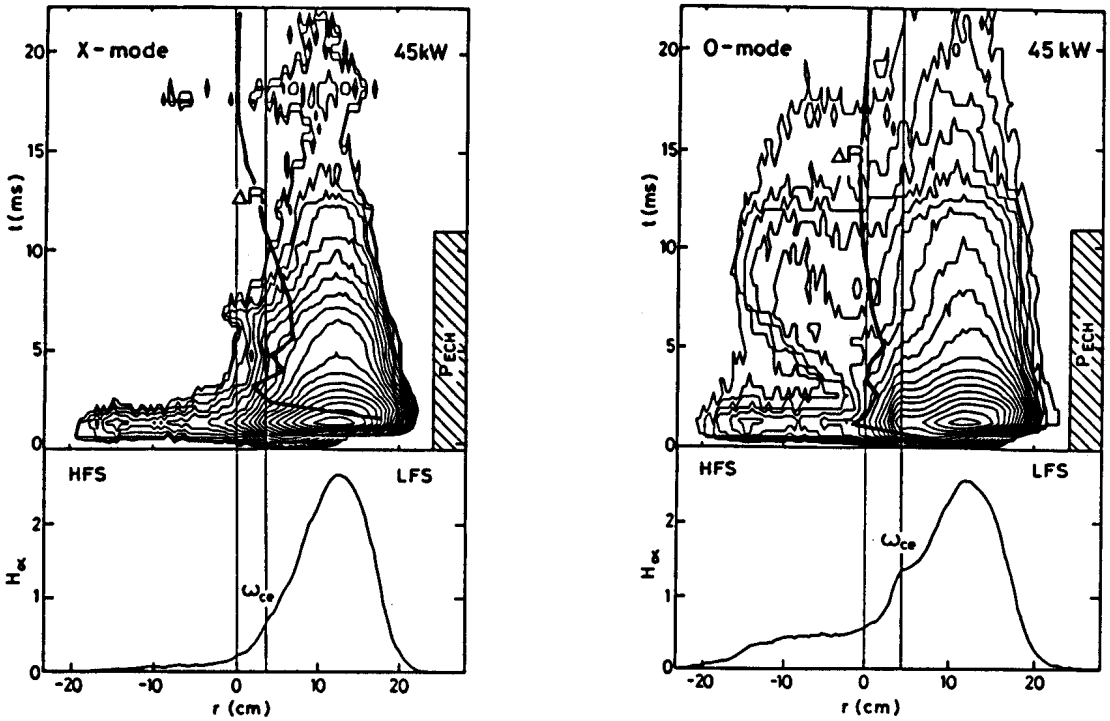

Fig. 2. H_α profiles and contours for (a) X-mode and (b) O-mode launch. Evidence of ω_{ce} absorption and current broadening is visible with O-mode launch. ΔR indicates current position during startup phase.

undetectable for X-mode launch. However, the dominant feature for both modes is a more intense broader peak on the low field side (LFS) of the ω_{ce} resonance in the region of the upper hybrid resonance (UHR)[3], which is seen to move further to the LFS for higher n_e. The presence of this peak, expected to exist only for X-mode launch, further indicates incomplete first-pass O-mode absorption followed by wall reflections and mode-mixing. In addition, X-mode startup vertical Bremsstrahlung profiles show a clear initial emission peak while O-mode startup shows a broad emission profile. This localised X-mode peak moves with magnetic field and mirror position as expected.

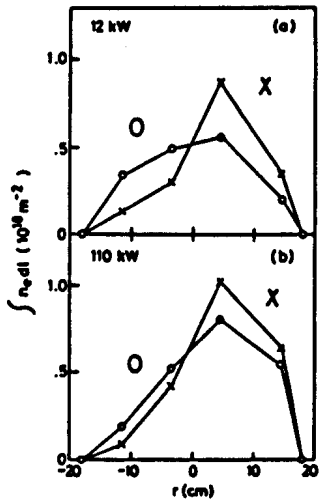

Fig. 3. Density profiles for (a) low power and (b) high power X- and O-mode launch. Density profiles are more peaked in X-mode and displaced further to the LFS with increased power.

Density profiles of Figs. 3 show that X-mode profiles are more peaked and further displaced to the outside. High-power X- and O-mode profiles show a significantly larger fraction of density to the LFS than low-power profiles as the absorption location moves with the UHR. O-mode density profiles, however, always remain broader and more centrally located as the ω_{ce} resonance remains fixed and the density rises more slowly.

Carbon-IV line burnthrough times indicate an initial heating rate twice as high in X-mode, as shown later in Fig. 5(c). A further indication that higher electron temperatures are produced during X-mode launch is given by the systematic need for higher gas injection for X-mode to maintain low runaway populations.

Startup characteristics

The different spatial absorption characteristics of X- and O-mode launch influence startup current position. Figure 4(a) shows that strongly localised LFS-UHR X-mode

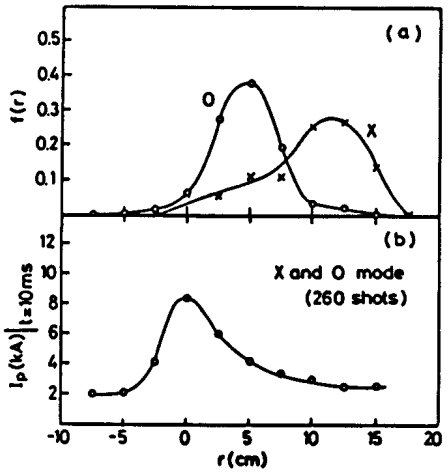

Fig. 4. (a) Distribution of startup current position for X- and O-mode showing a more central startup for O-mode. (b) Startup current vs. current position showing advantage of centrally started current. Tokamak feedback control is set for central current positioning. This curve is independent of X- or O-mode launch.

absorption initially creates a highly non-centered plasma. O-mode launch, however, by creating more centrally located absorption profiles allows the current to start near the center. Figure 4(b) shows the advantage of a centrally located startup current. Independent of the mode launched, currents starting nearer the center of the poloidal cross section (result of O-mode injection) experience significantly higher current ramp rates than those starting nearer the LFS (result of X-mode injection).

The dependence of startup on plasma current location is reflected in the current ramp rates for a series of X- and O-mode startup shots at varying ECH powers (*5-110kW*). In this series the ω_{ce} resonance is close to axis. Figures 5(a-b) show the

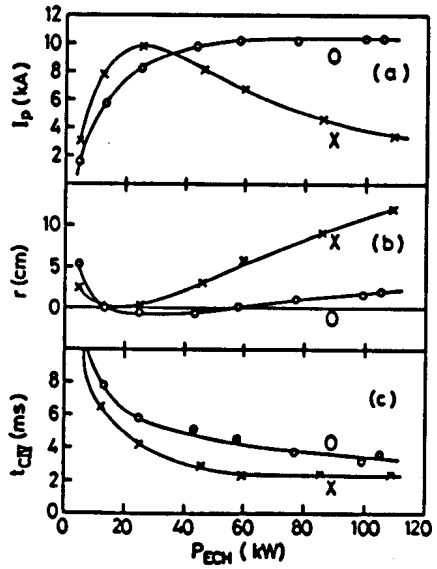

Fig. 5. X/O-mode, ECH-assisted startup power series showing (a) plasma current at end of ECH pulse, (b) corresponding radial plasma position, (c) carbon-IV burnthrough times.

plasma current attained by the end of the ECH pulse and the corresponding current center. The degraded startup performance of X-mode launch at high ECH power can be attributed to the movement of the current center to large r as power is increased. This displacement is consistent with the density profile changes caused by strong X-mode absorption near the UHR layer which moves to large r as ECH power, and thus electron density, increases. The current center for O-mode launch also moves to larger r with increasing power but the broader absorption profile allows it to remain near the axis over

the entire power range. At constant power, the average current ramp rate is independent of r_{res} for $-9cm < r_{res} < 4cm$[4].

Well-sustained discharges are characterised by a spreading of the H_α emission from the center to the HFS attesting to the formation of a hot plasma across the entire cross section. Discharges which do not develop this feature are not sustained at ECH turn off. The H_α emission of sustained discharges develops into the usual radiative halo.

Loop voltage and volt-second saving

These ECH-assisted startup studies generally use a constant loop voltage of $1.2V < V_L < 2.1V$ chosen to minimise volt-second consumption while still creating acceptable current ramp rates. Minimum startup loop voltage values reached $V_L = 0.6V$ ($E=0.15V/m$), compared to the minimum required 8V for purely inductive breakdown in TCA. Figure 6 shows significant volt-second saving over standard ohmic startup for $\Delta t_{ECH} > 20ms$. At $\Delta t_{ECH} = 40ms$, volt-second saving reaches 35% of that of ohmic startup.

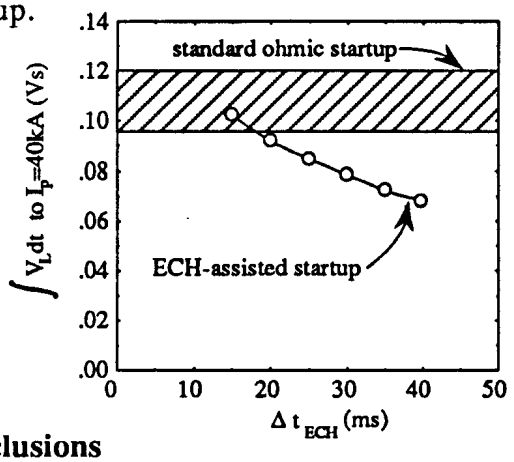

Fig. 6. Volt-second consumption for ECH-assisted and ohmic startup to 40kA. ECH startup values are shown for varying ECH pulse lengths for 60kW, O-mode launch. Total available flux on TCA is .48Vs.

Conclusions

In these startup experiments, X-mode launch has never exhibited better current rampup properties than O-mode, although its absorption properties are seen to be far better. X-mode experiences highly localised first pass absorption near the UHR layer, creating a peaked absorption profile at large r. O-mode launch, on the contrary, is less efficiently absorbed and creates a broader absorption profile after wall reflections and mode mixing. The practical superiority of O-mode launch is attributable to the more uniformly spread power deposition which allows rapid current rampup over a much wider range of operating conditions. Low loop voltage startup has been achieved for $V_L = 0.6V$ and significant volt-second saving over standard ohmic startup is seen for ECH pulse lengths of $\Delta t_{ECH} > 20ms$.

Acknowledgements

The authors acknowledge the support of the TCA and gyrotron teams. This work was partially supported by the Fonds National Suisse de la Recherche Scientifique.

References

1 A. Pochelon, T. Goodman, D. Whaley, M.Q. Tran, et al.16th. Symp. on Fusion Technology, London (1990).

2 B. P. Duval, to be published.

3 R. M. Gilgenbach et al., Nucl. Fus. 21 (1981) 319.

4 B. Lloyd, T. Edlington et al., 13th EPS on Contr. Fus. and Plasma Heating, Schliersee, Vol. 10C, PartII (1986) 266.

MEASUREMENT OF ION TEMPERATURE PROFILES IN THE TCA TOKAMAK BY COLLECTIVE THOMSON SCATTERING

C.Nieswand, R.Behn, M.R.Siegrist, M.Dutch, B.Duval, A.Pietrzyk, A.Pochelon

Centre de Recherches en Physique des Plasmas
Association Euratom - Confédération Suisse
Ecole Polytechnique Fédérale de Lausanne

1. Introduction

After many years of development in the field of plasma diagnostic techniques, local ion temperature measurements in tokamak plasmas are still rather difficult. Neutral particle analysis (NPA), e.g., although it is a line integrated measurement, provides approximately the maximum temperature along the line of sight. But the result is influenced by charge exchange cross-sections, the neutral particle distribution and, with our system at TCA, by the H-D composition of the plasma.

It has been shown, that collective Thomson scattering in the far infrared is capable of measuring ion temperatures in tokamak plasmas with good spatial and temporal resolution [1]. Nevertheless, the result depends on other plasma parameters which must be determined simultaneously.

The collective Thomson scattering system on TCA has been modified to allow measurements of the spatial ion temperature profile in the central part of the plasma. The results are presented and compared with NPA temperature profiles measured in similar TCA plasmas.

2. Experiment

The source for the collective Thomson scattering experiment is an optically pumped D_2O laser with 0.5-1 MW power within 1.5μs at 778.47 GHz. The beam is focussed vertically into the plasma and the scattering volume of 3mm diameter is observed under nearly 90°. The solid angle of observation is about $4.3 \cdot 10^{-3}$ sr. This results in a scattered power of the order of 10^{-19} W/Hz. A heterodyne detection system was developed to obtain spectral resolution at such a low signal level. An optically

pumped CW CD_3Cl laser at 782.17 GHz with 1mW CW power serves as a local oscillator and is focussed together with the scattered light onto a Schottky barrier diode mixer. A 12 channel spectrometer analyzes the difference frequency with 80 MHz resolution.

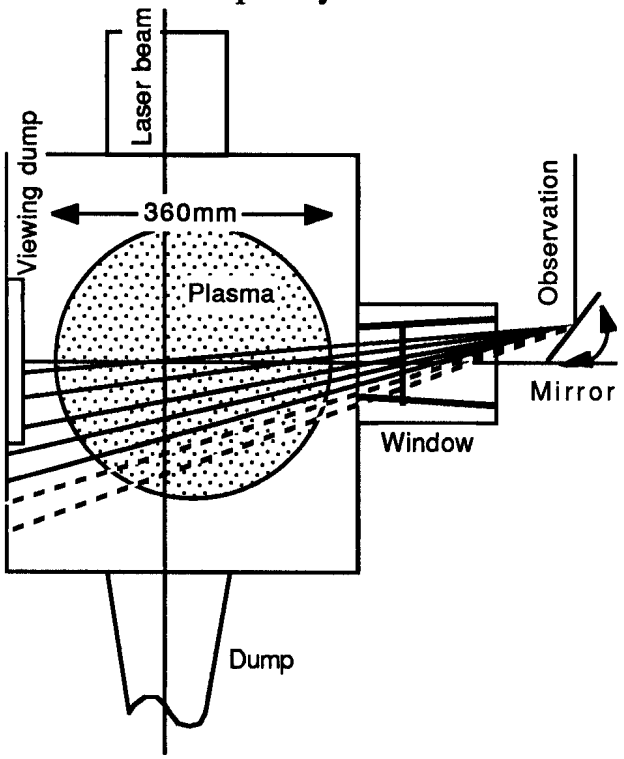

Fig.1: Scattering geometry

The position of the scattering volume could be changed by tilting the first focussing mirror in the detection optics (see fig.1). This allowed observation of the profile from the plasma centre to 2/3 of the plasma radius. Of course the scattering angle and the angle between the scattered wave vector k_s and the magnetic field B are different for each radial position. The influence of the latter can become very important when it approaches 90°. In this particular case, the spectrum is dominated by structures induced by the magnetic field. It was verified in this experiment, that this angle was always smaller than 87° so that the influence of the magnetic field was kept small.

A radial profile was built up from a series of reproducible tokamak discharges, and each temperature value in figure 2 is an average over 2 or 3 shots.

The evaluation of the spectra requires the knowledge of additional plasma data. The electron temperature was provided by incoherent Thomson scattering using a ruby laser. A q profile was derived from these data, from which the angle between k_s and B could be determined. The electron density was measured by a 4 channel FIR interferometer. The impurity concentrations were asumed to be uniform over the plasma radius with 2% carbon, 1% oxygen and 0.2% iron, corresponding to a Z_{eff} of 2.5.

All measurements were performed in high density deuterium discharges ($n_e \approx 10^{20} m^{-3}$) to obtain acceptable signal to noise ratios. Such discharges could be produced in TCA with high reproducibility by hard gas puffing. The plasma current was kept constant while the density was in the transient phase.

In a series of comparable discharges the line of sight of the neutral particle analyser was scanned vertically over the plasma minor radius. Thus, we could compare T_i measurements from two different diagnostics methods.

3.Results

T_i profiles measured by collective Thomson scattering and by neutral particle analysis are shown in figure 2. The corresponding T_e profile from ruby Thomson scattering is included. It has a central value of about 750 eV and is clearly peaked. The data from the collective Thomson scattering reveal a flat profile with a nearly constant T_i value of about 400 eV in the observed part of the plasma and crosses the Te profile at one half of the minor plasma radius. In the outer part of the plasma T_i seems to be larger than T_e. This means, together with the facts that the central temperatures are very different and the equipartition time is very short (<10μs), that the radial ion heat transport must be very large. However, the NPA results show a significantly lower value of about 300eV. It indicates, that T_i is not significantly larger than T_e in the outer parts of the plasma, but both temperatures are equal at r=100mm.

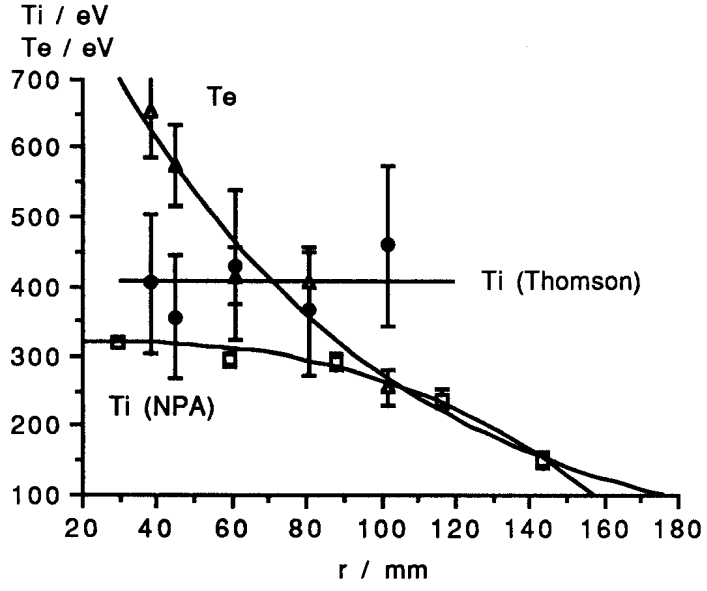

Fig 2: Measured temperature profiles in a high density plasma during hard gas puffing, 130ms after breakdown

The confidence interval for the ion temperature measured by collective Thomson scattering was analyzed with Monte Carlo simulations and can reach about 12% for densities of $10^{20}m^{-3}$ and for a single shot, if the 12 channels of the spectrometer are tuned to the optimum part of the spectrum of the scattered light [2].

For these calculations uncertainties of 5% for n_e, 10% for T_e, 30% for the impurity concentrations and 10% for the magnitude of the magnetic field were assumed.

Unfortunately, the number of spectral channels used had to be reduced because stray light dominated the scattered light in the most central spectral channels. The stray light became large during measurements at outer radial positions, when the detector looked directly on the metal wall of the tokamak vessel and not on the ceramic viewing dump. This increases the uncertainty considerably. With only 11 channels the uncertainty grows up to 25% [2] and even exceeds this value when less channels are used.

The statistical error for the NPA measurements was found to be about 8%. The NPA might give systematically too low temperatures, because the result is a weighted average over all temperatures along the line of sight. The existence of hydrogen released from the wall imposes another systematic error on the NPA measurement, because the system is calibrated to deuterium.

Within these errorbars the results of both diagnostics are comparable. The form of the profile in this region is flat in both cases.

The observation of peaked T_e and flat T_i profiles is consistent with results obtained in other tokamaks with comparable parameters [3,4,5]. It should be noted that our measurements refer to discharges with $n_e \approx 1 \cdot 10^{20} m^{-3}$, whereas most of the results given in [3,4] have been obtained at considerably lower central densities ($2\text{-}5 \cdot 10^{19} m^{-3}$).

4. Conclusion

It was shown that the measurement of T_i profiles can be performed by collective Thomson scattering. The results are consistent with NPA measurements in the range of the errors of these diagnostics. It was found that in high density TCA dischargesT$_i$ might be larger than T_e in outer parts of the plasma . This implies a large radial ion heat transport.

References :

[1] R.Behn, D.Dicken, J.Hackmann, S.A.Salito, M.R.Siegrist, P.A.Krug, I.Kjelberg, B.P.Duval, A.Pochelon; Phys.Rev.Lett. 62, 2833 (1989)

[2] M.R.Siegrist, R.Behn, D.Dicken, B.P.Duval, J.Hackmann, B.Joye, J.B.Lister, C.Nieswand, A.Pochelon, D.C.Yuan; J.Appl.Phys. 69, 1993 (1991)

[3] D.Dimock, D.Eckhartt, H.Eubank, E.Hinnov, L.C.Johnson, E.Meservey, E.Tolnas, D.J.Grove ; Proc. 4th conference on Plasma Physics and Controlled Fusion Research in Madison, 451 (1971)

[4] L.A.Berry et al. ; Proc. 6th conference on Plasma Physics and Controlled Fusion Research in Berchtesgaden, Vol.I, 49 (1976)

[5] TFR Group ; Proc. 7th Fusion in Lausanne, Vol.I, 2 (1975)

Density Limit Studies in the TCA Tokamak.

Z.A. Pietrzyk, R. Behn, A. Bondeson, B. Duval, P.-A. Duperrex, B. Joye, A. Knight, B. Marchal, C. Nieswand, A. Pochelon

Centre de Recherches en Physique des Plasmas
Association Euratom-Confédération Suisse
Ecole Polytechnique Fédérale de Lausanne
21 av. des Bains, CH-1007 Lausanne Switzerland

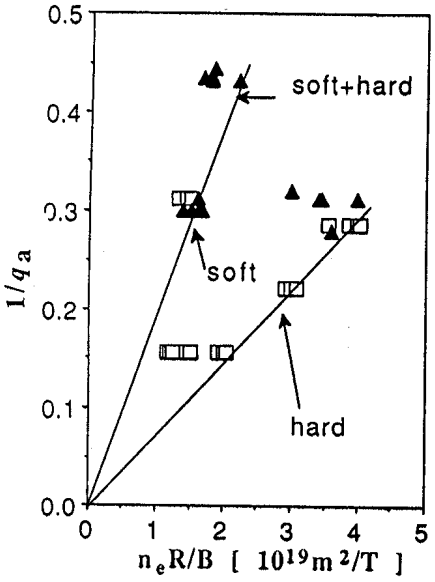

Fig. 1 *Hugill diagram; the squares are shots with mode limited density, the triangles are shots which disrupted.*

In the TCA tokamak the density can be limited either by disruptions or increased mode activity. The density is limited at two different values depending on the operation. Determinant parameters are the edge q value, q_a, and the way the gas is fed to the plasma. From a large number of possible scenarios of tokamak operation, we selected two for this study which we call soft and hard gas puffing. These two scenarios produce different kinds of disruptions and, for $q_a > 3$, have different density limits. Soft and hard puffing are both produced by programming a step function gas input to the vacuum chamber, the difference being the size of the step. Hard puffing gives rise to a temporal maximum in the soft X-ray signal at the beginning of the hard puff, a sudden increase of $\beta + l_i/2$ and moderate mode activity[1]. In soft puffing the first two of these signals are monotonic functions of time, while mode activity starts at a low level and grows before the disruption.

The two density limits and the different limiting activities can be seen in the Hugill diagram (Fig. 1). Soft puffing is not sufficient to reach the limit expected from Greenwald[2] scaling whereas hard puffing is. We have observed differences in the nature of disruptions during soft and hard puffing discharges. We will describe these differences and the physical processes leading to disruptions in both cases.

The first difference observed is the time evolution of the mode frequency measured by magnetic probes (Fig. 2). A soft puff produces the "normal"[3] mode behaviour, with a frequency which decreases with time. Hard puffing shows a rather rapid increase in mode frequency at the beginning of the puff which then remains almost constant until the disruption. The hard puffing mode frequency before disruption is as high as in soft puffing in the beginning of the discharge and is double the soft puffing mode frequency just before disruption. The mode frequency is a function of the diamagnetic drift velocity, which depends on the pressure gradient. The pressure gradient at $q = 2$ (the mode has $(m,n) = (2,1)$ and $(4,2)$) is smaller for soft than hard puffing, which was verified by Thomson scattering measurements. In addition, the plasma inductance for soft puffing is either constant or slightly increases with time. For hard puffing it reaches a maximum at the beginning of the puff and decreases later until disruption. The hard puffing shows an acceleration of the mode frequency a few periods before the disruption (see Fig. 3), which indicates that wall stabilization of the mode, before disruption, is not effective at this frequency.

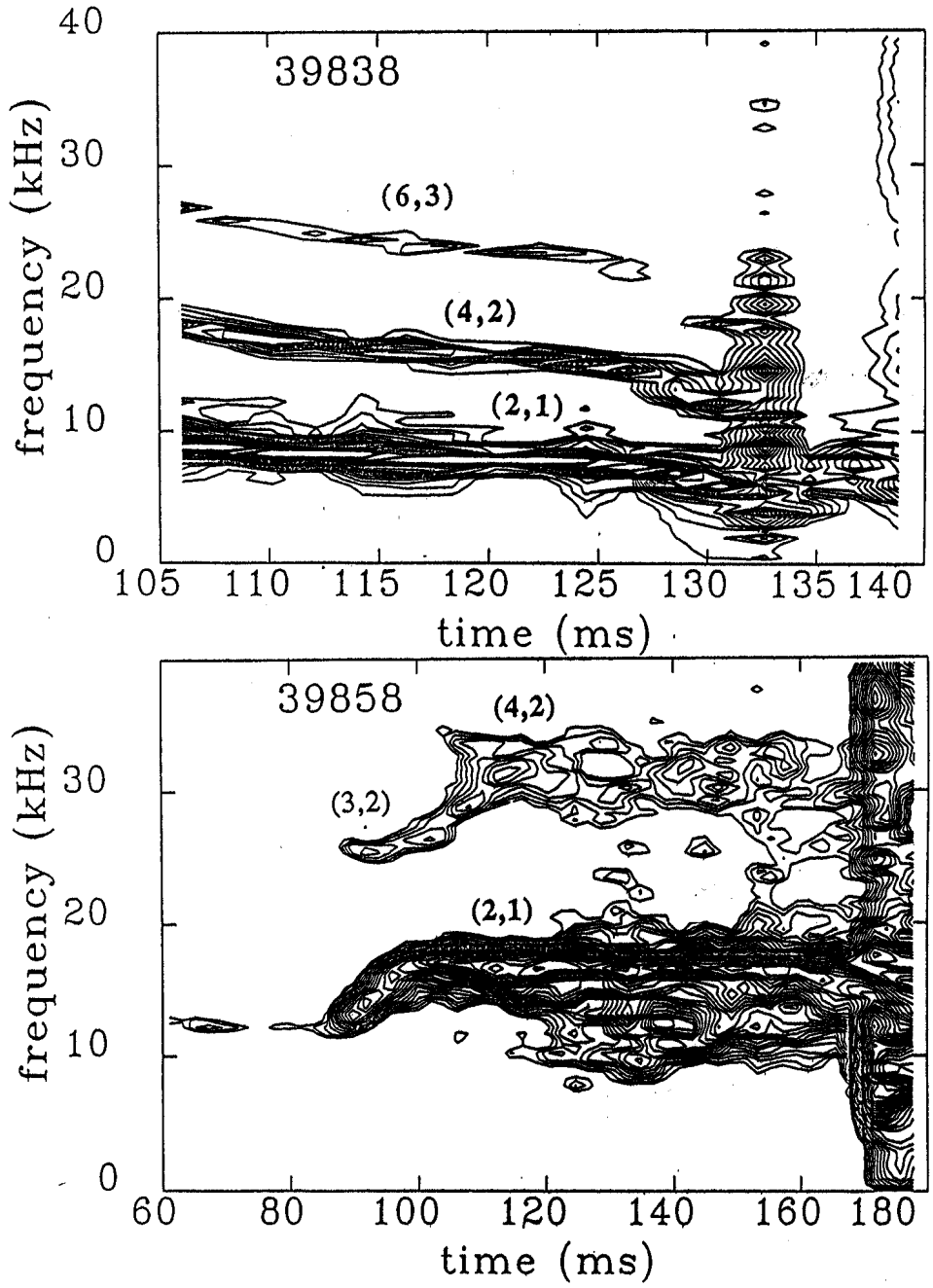

Fig. 2 *Isoplot of frequency versus time for soft puffing (top) and hard puffing (bottom) discharges, gas puff starts at 75 ms. In brackets are the (m,n) mode numbers.*

The upper part of the empirical l_i versus q stability diagram for TCA (Fig. 4) indicates that the maximum l_i during hard puffing crosses the unstable region. The differences in the temperature, pressure and neoclassical current density profiles, for soft and hard puffing before disruption, are within the error bars of the Thomson scattering measurements. This suggests that in both soft and hard puffing we reach the same instability region but from different directions with respect to the plasma inductance. The plasma inductance increases with time for soft puffing discharges while for hard puffing it decreases before disruption.

In Fig. 4 the range of the instability region is shown only schematically. We did not investigate the unstable region to see its real extension along the l_i axis. For $q_a < 3$ the instability gap could not be crossed using the standard hard puffing method and the density limit was the same for both soft and hard puffing.

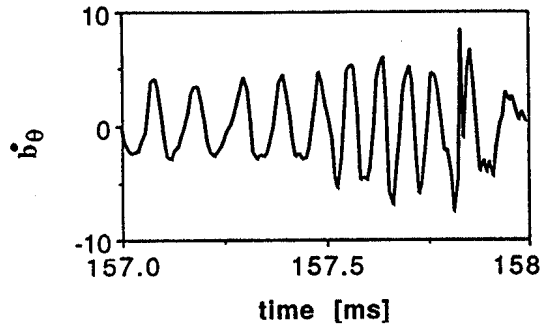

Fig. 3 *Magnetic oscillations just before disruption for hard puffing discharge.*

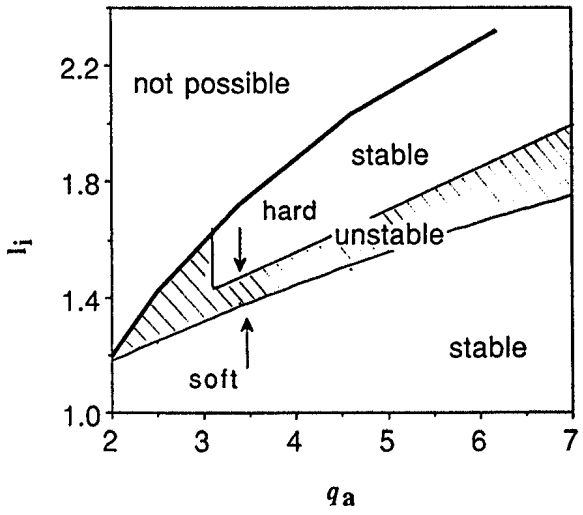

Fig. 4 *Upper part of empirical stability diagram for TCA. Stable and unstable regions in l_i versus q_a.*

At this moment one could say that the soft puffing disruption is a "normal"[3] disruption although the loop voltage starts with a *positive* loop voltage spike. This peculiarity is present only for disruptions with soft puffing at $q_a > 3$, suggesting that there is no sudden redistribution of current at the start of the disruption. For $q_a < 3$ the disruption always starts with a negative loop voltage spike for soft as well as for hard puffing.

In both hard and soft puffing the disruption starts at the $q = 2$ surface (indicated by a spike on the multi-channel soft X-ray signals near r=14 cm). The disturbance moves towards the centre, often very rapidly, and destabilizes the $q = 1$ surface. It then moves in both radial directions and from this point the soft X-ray flux diminishes. This is not related so much to the reduction of central electron temperature (which judging from a few Thomson scattering temperature profiles is almost the same before and just after disruption), as to a reduction of the total plasma energy, which shows a significant drop just after a current disruption. The temperature profile becomes narrow and the deterioration of current starts from the outer region of the plasma.

The approach to the instability from high to low plasma inductance in hard puffing discharge is an important difference in the physics of disruption.

We attempted to check experimentally whether the initiation of a hard puffing disruption was linked to a broadening of the current profile, by trying to delay the disruption using a second hard puff. If the approach to the instability is from high inductance, the second puff would delay it, as it increases inductance by cooling the plasma edge. On the other hand, the approach from lower inductance would accelerate it. The second puff was programmed at 140 ms in discharges with reproducible minor disruptions at 160 ms. The second puff delayed the disruption by 15 ms and increased the line density by 25% before disruption. This experiment shows that the approach to the unstable region in hard puffing operation is from peaked to broad current profiles.

For $q_a > 3$ the density can be limited either by disruption or by increased mode activity. For $q_a \geq 4.5$, the density is only limited by mode activity without a plasma current disruption. In such cases the mode frequency also initially decreases. This can be interpreted as a flattening of the pressure profile near a rational surface. The modes start with $(m,n) = (3,1)$, indicating a perturbation at the $q = 3$ surface. This mode is stabilized by hard puffing and its amplitude is reduced. A little later, a (2,1) mode starts to grow. It has a lower frequency. The change in mode is clearly visible in Fig. 5 as a sudden jump in frequency at 90 ms. The presence of large mode increases particle and energy losses from the plasma edge. One can speculate that this mode grows until it is strong enough to expel particles from the plasma, resulting in a reduction of the density mostly from outside the q=2 surface. It can be assumed that these losses produce more peaked current profiles, a

situation resembling hard puffing but without the density increase. This reduces the plasma pressure outside the $q = 2$ surface, increasing the pressure gradient at that surface, which increases the diamagnetic drift velocity and leads to gradually increase in the mode frequency. The mode frequency increases and the plasma returns to the state before the mode started to grow.

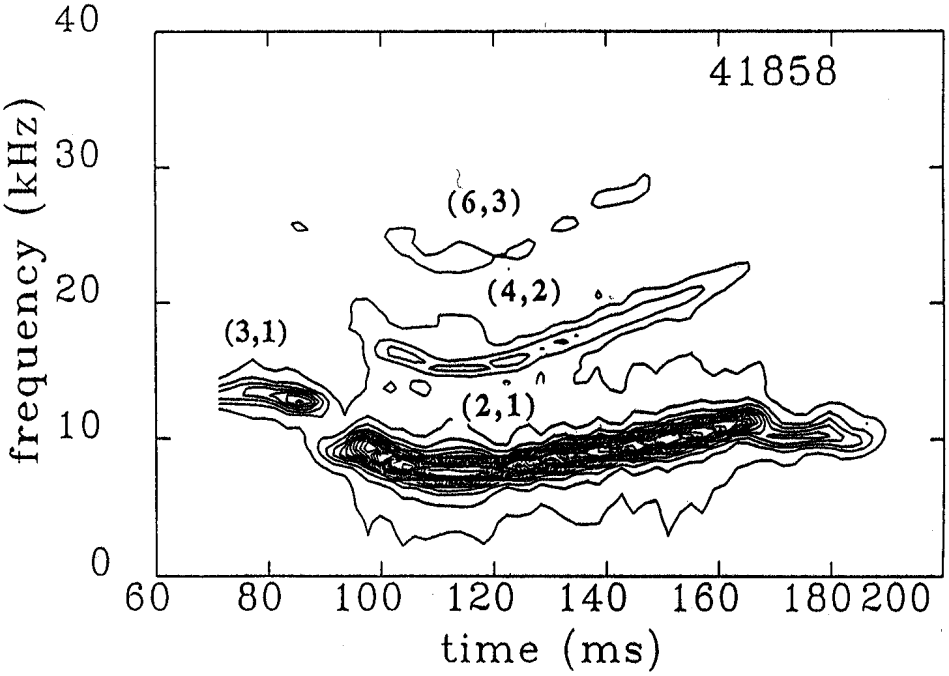

All of these results do not depend strongly on the purity of the plasma even though the radiation losses were quite different over the various experimental series. At the hard puffing density limit the radiative losses were equal to the Ohmic input power and the radiation profile was peaked.

Fig. 5 *Isoplot of frequency versus time for hard puffing q_a =4.5 with density limited by mode activity. Gas puff starts at 75 ms. In brackets are the (m,n) mode numbers.*

However, for less pure plasmas the total radiated power reached the Ohmic power at the (lower) soft puffing density limit. Hollow radiation profiles at high density and with dirty plasmas suggest that the increased radiation was from low Z ions which increased the radiation near the plasma edge. It is interesting to note that the toroidal beta reached 62% of the Troyon limit, $\beta_{Troyon} = 2.2\ \mu_0 I_p\ a\ /\ B$ [%], with only Ohmic heating at the hard puffing density limit.

Finally, one has to mention dramatic, spectroscopically measured, changes in rotational ion velocity [4]. Poloidal increase and toroidal decrease during hard puff injection discharges. This suggests increased radial electric field in these discharges. We do not know, whether these effects in any way change the plasma stability, thereby preventing disruption at high l_i values.

[1] Ch. Nieswand, Z.A. Pietrzyk, A. Pochelon, R.Behn, A. Knight Controlled Fusion and Plasma Heating Amsterdam Part I p 78 (1990).

[2] 3. M. Greenwald et al, A New Look at Density Limits in Tokamaks MIT report PFC/JA-86-22 (1988)

[3] J.A. Wesson et al Nuclear Fusion 29 641 (1989)

[4] B.P. Duval, B.Joye, B.Marchal Measurements of Toroidal and Poloidal Rotation in TCA. Paper at this conference

THE GENERATION OF HARMONICS AND THE COUPLING BETWEEN MHD ACTIVITY AND THE FUNDAMENTAL FREQUENCY DURING ALFVEN WAVE HEATING IN TCA

G.G.BORG P.A. DUPERREX and J.B. LISTER

Centre de Recherches en Physique des plasmas
Ecole Polytechnique fédérale de Lausanne
21 Av. des Bains, Ch-1007, Lausanne, Switzerland

1. Harmonic Generation During Alfvén Wave Heating

During Alfvén Wave Heating (AWH) at 2.5 MHz in TCA (ω_{ci} = 11.5 MHz), harmonics are observed on the wavefields in the plasma scrapeoff layer (SOL). The spectrum of harmonics consists predominantly of signals at frequencies that are integer multiples of the fundamental. No evidence for half-odd integral harmonics has been observed and harmonics are not observed at very low power. It is generally believed that the harmonics observed in the SOL during ICRH are due to a sheath effect at the antenna [1]. In our experiments, the possibilities of wave excitation by shielded and unshielded antennas [2] and the measurement of the rf Langmuir current (fault current) [3] flowing between an unshielded antenna and the plasma, permit us to provide a definite conclusion about the relevance of this mechanism in AWH.

In TCA there are four pairs of top and bottom antennas equally spaced toroidally. These permit antenna phasings with toroidal mode numbers N = 1, 2 and 4 and poloidal mode numbers M = 0 and 1. In Fig. 1 we show magnetic wavefield traces of the fundamental (f_0) and first harmonic (f_1 = 4.98 MHz) for four phasings (N,M) of the antennas. The peaks are resonances of the discrete Alfvén wave (DAW) [4]. We note that the DAW spectrum versus density is remarkably similar for f_0 as for f_1. The amplitude of f_1 is generally between 2 and 10 times lower than f_0. All harmonic spectra show resonances of the DAW. Experiments in which the toroidal field was lowered showed that the resonance densities of f_0 and f_1 were always the same; in the case of (2,1) excitation, the f_1 peak was present above the ion cyclotron frequency. In addition, although there is some evidence of DAWs excited directly at the harmonic in these traces, DAWs at f_1 were generally not observed. From this we conclude that the peaks in the harmonic traces are plasma responses to the DAW peak in the fundamental.

Finally we note that similar traces are observed even if only one antenna pair is excited, whether or not the antennas are screened.

The fault current driven from an excited antenna to the SOL, which is totally eliminated by screens, tends to follow the antenna voltage and does not have the detailed DAW structure evident in Fig. 1. Its amplitude is typically about 5% of the circulating current (≈ 1000 A) although as previously noted [3] it is difficult to measure when the antenna is excited symmetrically. The power structure in the f_0 trace arises from the change in the angle between a structureless circulating antenna current and antenna voltage. In an earlier paper [3] however, it was shown that the fault current is in phase with the driving voltage so that power dissipation by the fault current must also be structureless. We conclude that the fault current and hence a sheath effect at the antenna is not the source of the harmonics.

The fault current driven passively in the matching circuitry of an unexcited antenna, just like the rf component of the Langmuir probe saturation current (I_{sat}) and floating potential, does have the DAW structure whether or not waves are excited by shielded or unshielded antennas. It is possible that harmonics are generated by the passive fault current driven at the fundamental in unexcited antennas, limiters and perhaps even at the vessel wall by fluctuations in the SOL potential. This is a difficult hypothesis to check and it is difficult to imagine that it would compete with the active fault current. The current flowing to the vessel wall was measured to be negligible compared to that flowing to an unshielded antenna; typically a few amperes. An experiment with excitation of the earthed shielded antenna pair in which two pairs of unshielded antennas were disconnected showed that, despite a reduction in the total passive fault current by a factor of two, there was no observable change in the amplitude of f_1 with respect to f_0 measured on the edge wavefields. In this experiment though one is never certain that a non-negligible part of the passive fault current has been eliminated.

We have given strong evidence against a sheath effect at the antenna (and perhaps anywhere) being responsible for the production of harmonics in AWH. The relative amplitude of the fundamental and harmonics appears to suggest that MHD nonlinear effects are not possible. Further studies are being made to investigate the possibility of electrostatic effects in the SOL during AWH.

2. Coupling Between MHD Activity And Alfvén Waves.

It has been observed that frequency spectra of the RF field associated with the Alfvén waves exhibit side-bands around the fundamental frequency (2.5MHz). Analysis of magnetic pick-up coil signals was undertaken to understand their origin and what information could be extracted concerning, for instance, MHD activity and turbulence.

For the broadband magnetic turbulence, test of 3-wave coupling between the side-bands and the low frequency signals has been performed using the bicoherence analysis on fast digitized data (sampl.f≤32MHZ). No positive results have been obtained. A new function t was calculated to test if the side-bands were due to an pure amplitude modulation: $t(f,\Delta f)=\frac{E(X_-(f,\Delta f)\cdot X_+(f,\Delta f))}{E(|X_-(f,\Delta f)|^2)^{0.5}\cdot E(|X_+(f,\Delta f)|^2)^{0.5}}$ where $X_\pm(f,\Delta f) = Y(f\pm\Delta f)\cdot Y^*(f)$, Y(f) is the Fourier spectrum and E(Z) denotes an ensemble average over several spectra. The results indicate that the sidebands cannot be simply explained by an amplitude modulation. Demodulation experiments show that Mirnov activity is also visible on the demodulated sine and cosine signals, indicative of a coupling between the Alfvén waves and the MHD activity. In the Fourier spectrum of the demodulated signal, the Mirnov peak location varies with the Alfvén resonance conditions as shown in Fig.2. The peak (at f≈15kHz) is in the upper sideband before the (2,1)DAW. At and after the (2,1)DAW, this peak is located in the lower sideband. At the (2,1)DAW, an additional peak at lower frequency compared to Mirnov is always observed (f≈9kHz in Fig.2), probably due to coupling with MHD activity in the plasma centre. Correlation between the sidebands and the directly measured low-frequency (f<500kHz) magnetic broadband fluctuations has only been observed in a few cases.

These results indicate that Alfvén sidebands contain information (by frequency modulation) about internal MHD activity and fluctuations, the nature of this information depends on the excited Alfvén mode. Such activity in the plasma centre is not always detectable by direct low frequency magnetic probe measurements in the plasma edge. If the coupling surface can be selected by launching an appropriate Alfvén mode and the combined measurements of several magnetic probes, it appears that the analysis of the sidebands should provide a measurement of internally located magnetic fluctuations.

Acknowledgements: We wish to thank the whole TCA team for its support. This work was partially supported by the Fonds National Suisse de la Recherche Scientifique

References.

[1] R. Van Nieuwenhove et al., IAEA Technical Committe Meeting on ICRH/Edge Physics, Garching bei München, October 1989, Fusion Engineering and Design.
[2] G.G. Borg and B. Joye, 17th European Conference on Controlled Fusion and Plasma Heating, Amsterdam, vol.13B part III, p.1179 (1990).
[3] G.G. Borg et al., 16th European Conference on Controlled Fusion and Plasma Heating, Venice, vol.13B part III, p.1199 (1989).
[4] G.A. Collins et al., Phys. Fluids 29(1986)2260.

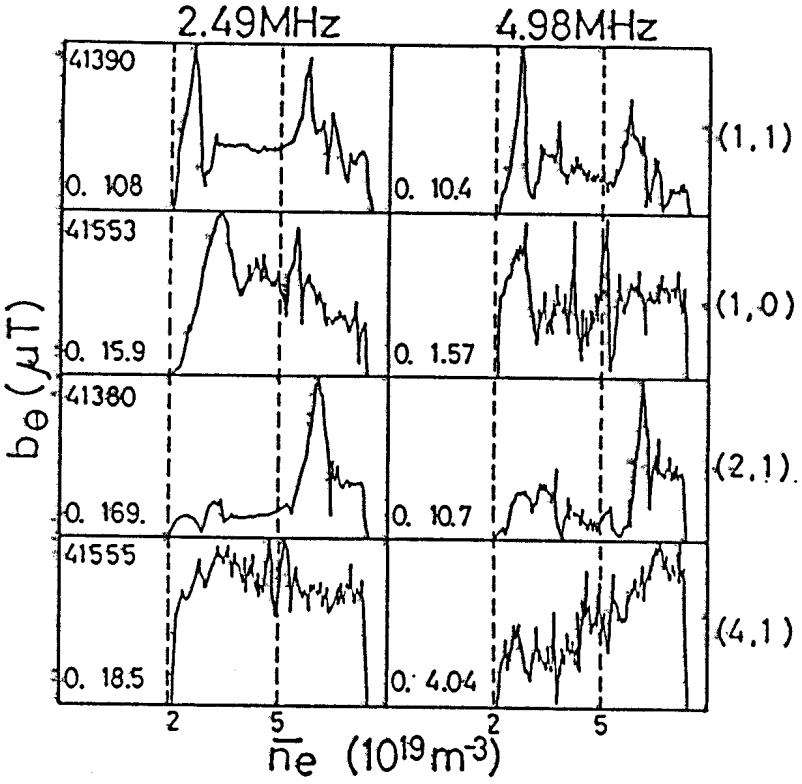

Fig.1:
RF magnetic field traces showing the DAW peaks in the fundamental and the corresponding peaks in the harmonic for various mode numbers (N,M). The scales are in μT.

Fig.2:
Time evolution of the Mirnov coil and demodulated signals.

2.a) Raw data.

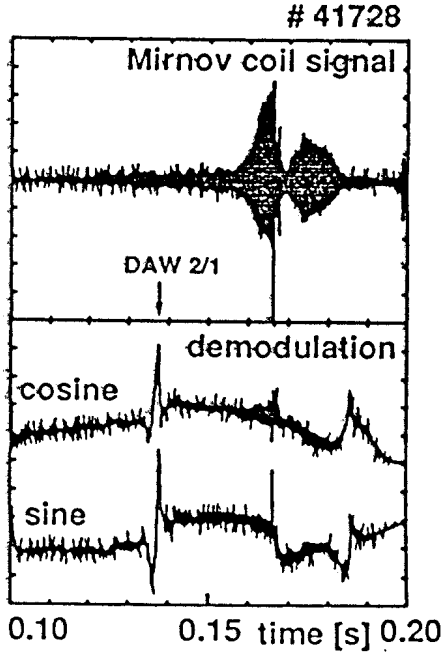

2.b) Power spectra. # 41728

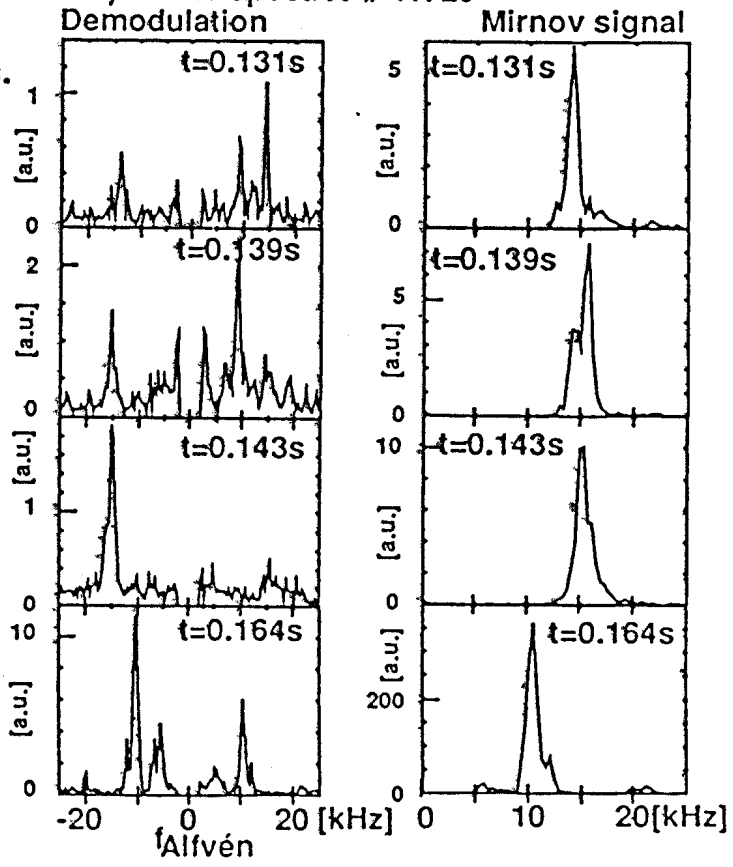

SIMULATION OF MHD ACTIVITY DURING DENSITY LIMIT DISRUPTIONS IN TOKAMAKS

A. BONDESON*, R. PARKER*
Centre de Recherches en Physique des Plasmas, Association Euratom - Confédération Suisse,
Ecole Polytechnique Fédérale de Lausanne, 21 Av. des Bains,
CH-1007 Lausanne, Switzerland

M. HUGON
JET Joint Undertaking, Abingdon, Oxon, OX14 3EA, United Kingdom

I. INTRODUCTION

The phenomenon of major disruption in tokamaks is well known, see, e.g. [1-3]. Despite detailed experimental studies, the theoretical understanding has remained poor. In this paper, we present numerical simulations and a theoretical model for major disruptions triggered by exceeding the density limit. The model contains as its main elements nonlinear mode coupling induced by the presence of a large amplitude m=2/n=1 mode and nonlinear interaction involving primarily the 2/1, 1/1 and 3/2 modes. Our model is consistent with the experimental observation that major disruption takes place in two steps: first an internal relaxation (termed 'profile erosion' [3]) flattens the temperature in the central region. In the second step, MHD turbulence develops, first in the $q \leq 2$ region, with a filamentation of the current and flattening of the q-profile. This leads to a final explosive growth of the $m \geq 2/n=1$ modes which flattens the entire current distribution and leads to a large drop in internal inductance.

The simulations on which our model is based use the reduced-MHD equations together with an equation for the electron temperature including ohmic heating, radiation losses and highly anisotropic thermal conduction. The radiation losses are prescribed so as to match measurements on JET during a density limit disruption (shot 11051 with $q_{cyl} \approx 5$) and a neoclassical formula for the resistivity is used [4]. A more detailed account of these simulations is given in [5].

II. PROFILE CONTRACTION - GROWTH OF PRECURSOR MODES

It is generally agreed that density limit disruptions are triggered by radiative energy losses which make the temperature and current profiles contract radially so that resistive MHD modes are destabilized. Observations on JET [3] show that the radiation losses are localized in a rather narrow layer that forms at the plasma edge and propagates inward. In shot 11051, magnetic perturbations of mode number m=3/n=1 and m=5/n=2 were recorded as disruption precursors when the radiation front passed over the respective resonant surfaces. We find in the reduced-MHD simulations that these modes can be excited to the observed amplitudes only by taking into account the effect of resistivity perturbations. (The radial magnetic field at the wall of the 3/1 mode reaches the rather high amplitude of 9 G.) Thus, the precursor modes are destabilized by a combination of current gradient driven tearing and resistivity gradient driven rippling. The rippling mechanism is effective as the temperature at the resonant surface is low at the time when the respective modes are excited.. The 3/1 pure tearing mode is at most close to marginal due to the strongly peaked and globally very stable current profiles resulting from neoclassical resistivity.

When the radiation front approaches the q=2 surface, the m=2/n=1 mode becomes strongly unstable and quickly grows to produce a magnetic island of about 20 % of the minor radius and a radial magnetic field at the wall of about 10 G. Because this mode is highly tearing unstable ($a\Delta' > 10$), its saturation amplitude is not much influenced by the resistivity

perturbations. For the continued simulation, all components except m = n = 0 of the resistivity have been turned off to avoid spurious manifestations of the rippling mode caused by numerical limitations on the maximum parallel thermal conductivity.

III. MINOR DISRUPTIONS

After the m=2/n=1 mode has reached high amplitude (with a saturated radial field at the wall ≈ 14 G), complex MHD activity follows in the simulations. A sequence of minor disruptions cause significant drops in the central electron temperature, but do not lead to major redistribution of the current profile. These q=1 minor disruptions are caused by resistive MHD instabilities whose fluid displacement is predominantly m=1/n=1. However, due to the coupling induced by the m=2/n=1 mode, the magnetic perturbation of these instabilities have m=3/n=2 components that are comparable to or even larger than the 1/1 component. Figure 1 shows the fluid and magnetic perturbations of a linear eigenmode with Fourier components m = 2n -1, n = 0, ±1, .., computed for a helical equilibrium with a q = 2 island of about 30 % of the minor radius (obtained from the nonlinear simulations just prior to a minor disruption).

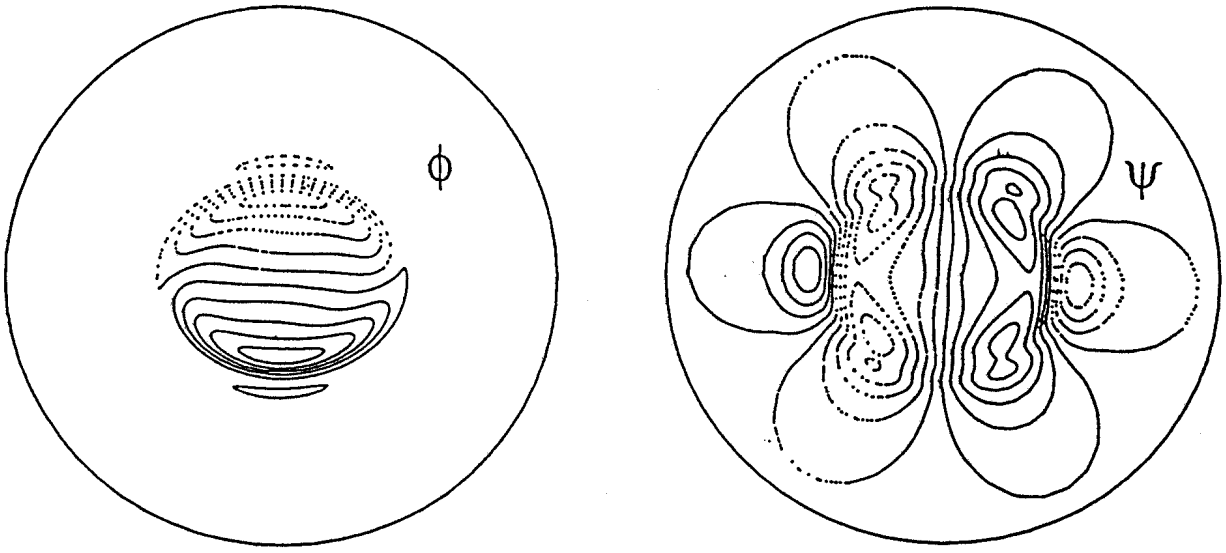

Figure 1. *Linear eigenmode on helical equilibrium with a large q = 2 island. Notice the dominance of m=1/n=1 in the displacement (ϕ) and of m=3/n=2 in the magnetic field (ψ).*

At the end phase of such a minor disruption, the large amplitude 2/1, 1/1 and 3/2 magnetic perturbations lead to stochastic magnetic fields in the entire region q ≤ 2. Field line stochasticity across the sharp current gradient between the q≈1 and q≈2 regions implies loss of equilibrium, and the simulations show MHD turbulence developing on the sharp current gradient. However, in a minor disruption, the turbulence never gets excited to high amplitude but decays away and the magnetic surfaces heal again.

We have established the importance of mode-coupling (as opposed to quasi-linear) effects by removing the nonresonant mode m=1/n=0 from the simulation. This significantly reduces the severity of the minor disruptions and completely eliminates the final major disruption.

IV. MAJOR DISRUPTION

In our reduced-MHD simulations, the major disruption takes place in two phases, in agreement with experimental observation [3]. The first phase is of the same nature as the q=1 minor disruptions. It is an internal relaxation with a mainly m=1/n=1 displacement and a strong m=3/n=2 magnetic perturbation due to coupling by the large m=2/n=1 mode. Invariably, this

internal relaxation starts from an initial condition in which the electron temperature is flat in the central q ≈ 1 region. Therefore, unlike a normal sawtooth crash, the m=1 fluid displacement does not lead to the motion of a peak in the temperature This can be seen from the one-dimensional cuts of the temperature profile in Fig.2, where the temperature falls on one side

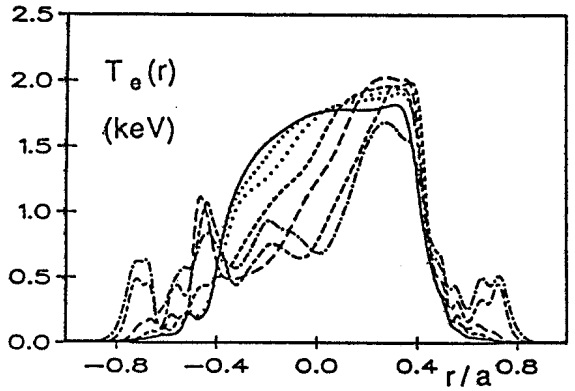

Figure 2. *One-dimensional cuts of the electron temperature during internal relaxation. (first phase of major disruption)*

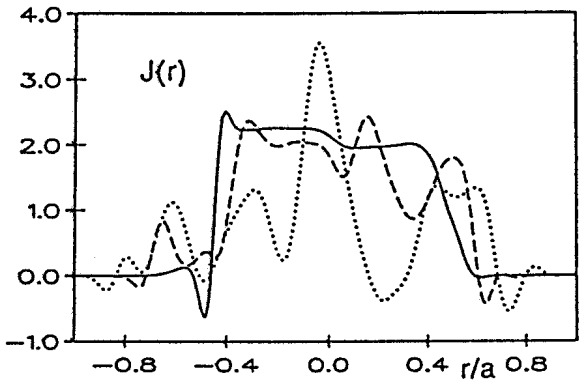

Figure 3. *One-dimensional cuts of the current density during current broadening (second phase of major disruption)*

but remains essentially constant on the other side during the internal relaxation. Similar behavior is observed experimentally [3, 6] during the so-called profile erosion in JET. Our interpretation that the temperature flattening is the result of an MHD instability with mainly m=1 displacement is, however, different from that of Ref. 3. At a certain stage of the internal relaxation, the presence of large amplitude 1/1, 2/1 and 3/2 magnetic perturbations (together with higher-m components) leads to a break up of the flux surfaces isolating the q ≈ 1 region from the q = 2 island and large-scale stochasticity develops in the region q ≤ 2.

As in the minor disruptions, stochasticity across the sharp current gradient between the q≈1 and q≈2 regions leads to MHD turbulence. It seems that there is only a slight difference between those internal relaxations that lead to minor disruption and that which continues into a major disruption with a large-scale broadening of the current profile. Notably, the amplitude of the 3/2 component becomes slightly larger in the internal relaxation that precedes the major disruption. In the second phase of the major disruption, the MHD turbulence triggered by the internal relaxation continues to grow. It involves many intermediate- and high-m modes and causes the central current profile to develop filaments.. The filamentation gradually flattens the q-profile inside q = 2 and finally the central q rises high enough so that the m=2/n=1 mode becomes strongly unstable. The 2/1 mode now grows explosively to high amplitude so that the q = 2 island encompasses the entire central region of the plasma. The 2/1 instability is followed by rapid instability of the 3/1 and 4/1 modes. During this final phase with fast growth of the m≥2/n=1 modes, the current profile broadens markedly and the internal inductance falls from close to 2 to about 1. One-dimensional cuts through the current profile during this final phase are shown in Fig. 3. The well-known negative voltage spike appears late in the disruption sequence, when regions of negative current occur near the plasma boundary. Following the instability of the m=4/n=1 mode, the magnetic field is stochastic over the entire plasma cross-section, which allows the hot electrons to leave the plasma on a time-scale of a few hundred

μsec. This mechanism for the final temperature drop is consistent with observations on e.g. TFR [1] with metal limiters, where the electron temperature falls quickly to about 200 eV and then evolves slowly. In JET with carbon limiters, the electron temperature falls to temperatures of the order of 10 eV [3], too low to be explained by conduction along stochastic field lines. Evidently, such low temperatures can be explained only by invoking atomic physics effects not modeled here.

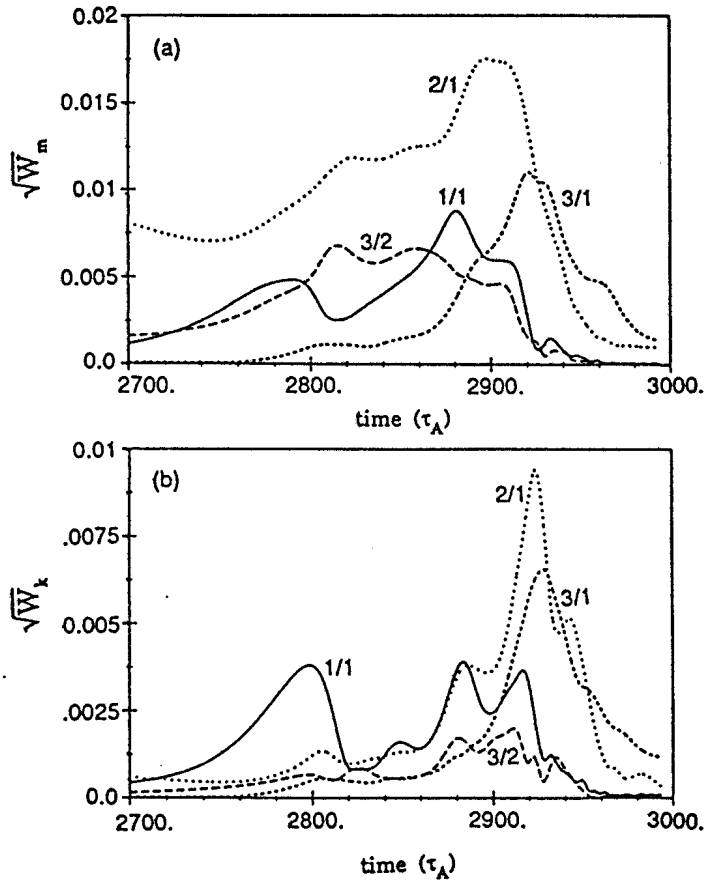

Figure 4. *Time histories of (a) magnetic and (b) kinetic perturbation amplitudes during major disruption. Note the separation into two different phases: internal relaxation and current profile flattening.*

A time history of the magnetic and kinetic perturbation amplitudes during the major disruption is shown in Fig. 4. This illustrates clearly the two phases of the disruption: first and internal relaxation occurs where the 1/1 component is dominant in the kinetic energy, followed by a hesitation, during which the 3/2 magnetic perturbation is significant, high-m modes are growing and the current profile develops filaments. In the final phase of the disruption, the m=2/n=1 mode grows rapidly to high amplitude.

*Work carried out under Article 14 contract JW8 / 9007 for JET Joint Undertaking.

REFERENCES

1. TFR Group, EUR-CEA-FC-1151, Nov. 1982.
2. F. Alladio, G. Bardotti, R. Bartiromo, *et al*, Nucl. Fusion **26**, 11 (1986).
3. J.A. Wesson, R.D. Gill, M. Hugon, et al, Nucl. Fusion **29**, 641 (1989).
4. S.P. Hirshman, R.J. Hawryluk, and B. Birge, Nucl. Fusion **17**. 611 (1977).
5. A. Bondeson, R. Parker, M. Hugon, JET-P(90)73, Dec. 1990 submitted to Nucl. Fusion.
6. P. Smeulders, private communication (JET, 1990).

FREE BOUNDARY TOROIDAL STABILITY OF IDEAL AND RESISTIVE INTERNAL KINKS

G. VLAD, Associazione Euratom-ENEA sulla Fusione, C.R.E. Frascati
C.P. 65-00044 -Frascati, Rome, Italy

H. LUTJENS, A. BONDESON, Centre de Recherches en Physique des Plasmas,
Association Euratom - Confédération Suisse, Ecole Polytechnique Fédérale de Lausanne,
21 Av. des Bains, CH-1007 Lausanne, Switzerland

I. INTRODUCTION

Recently, there has been a strong interest in the stability properties of the internal kink mode. This has been spurred mainly by experimental observations of sawtooth oscillations on large tokamaks revealing unexpected features such as double sawteeth with partial reconnection, fast crashes, and central q-values well below unity [1]. These observations are all difficult to reconcile with the conventional Kadomtsev model in which the crash is triggered by the resistive kink mode becoming unstable when the safety factor q falls below unity. The theoretical understanding of the sawtooth activity is made difficult by the sensitivity of the internal kink mode to several factors such as q-profile, pressure, resistivity, aspect ratio, shaping of the cross-section, and even wall position. In addition, the internal kink in a torus (with $q > 1/2$) is a rather weak instability and should therefore be sensitive to kinetic effects.

Here, we present results from a study of the resistive and ideal MHD properties of the internal kink mode. Generally, we have numerically computed growth-rates as functions of various parameters, using the full-resistive-MHD toroidal stability code MARS [2] and the cubic element equilibrium code CHEASE [3].

II. INFLUENCE OF THE CURRENT PROFILE

A major uncertainty for the understanding of the sawteeth is the shape of the current profile. Here, we restrict attention to circular cross-section with an aspect ratio of 4 and choose two types of current profiles. One has uniformly low shear inside a certain radius $r = r_p \approx 0.4a$, outside which the shear increases rapidly. The other has shoulders in the current profile which produce locally low shear near $q = 1$, while the central safety factor q_0 is well below unity. We refer to these as "low-shear" and "TEXTOR" profiles [1], respectively.

Figure 1 shows the low-shear current profile $j = \langle j_\phi \rangle(r)$ (where r is a flux surface label proportional to the square root of the enclosed volume). This current profile is monotone, but the shear $\hat{s} = (r/q)\, dq/dr$ has a slight local minimum at $r = r_p \approx 0.4a$, $\hat{s}(r_p) \approx 0.03$. The shear does not exceed 0.032 in the entire region $r < r_p$. Profiles of this type may arise in sawtoothing discharges if total reconnection occurs within the $q \approx 1$ region, $r < r_p$, followed by neoclassical peaking of the current during the rise phase [4]. We have considered a family of equilibria with self-similar current profiles where we specify the q-value at radius $r = r_p$. For this family, the central safety factor q_0 is related to $q_p \equiv q(r_p)$ by $q_0 \approx 0.948 q_p$. It may be useful to think of these equilibria as an approximation to the sequence in time during the ramp phase of a sawtooth, with q_0 and q_p decreasing functions of time. Figure 2 shows the resulting growth-rates for four different values of poloidal beta at the $q = 1$ surface (0.00, 0.05, 0.10, and 0.15) at Lundquist number $S \equiv \tau_{res}/\tau_A = 10^6$ (Fig 2a), 10^8 (2b) and 10^{10} (2c). For this q-profile, $q_p = 1$ locates the minimum shear ($s \approx 0.03$) at the $q = 1$ surface, and when q_p is decreased below unity, the $q = 1$ surface moves out into the region of high shear. For instance, $q_p = 0.98$ gives $\hat{s}(q=1) \approx 0.22$. In all cases shown in Fig. 2, a conducting wall is assumed at $r = b = 1.2a$.

We note from Fig. 2 that *complete* resistive MHD stability is very rarely achieved. However, in many cases, the resistive growth-rates are small, and we are led to the conclusion that a weak internal kink is stabilized for most of the sawtooth cycle by effects not included in the model. A likely candidate for such stabilization is diamagnetic rotation. In present day tokamaks, ω_*/ω_A is typically between 0.5×10^{-3} and 10^{-2}, which is comparable to resistive

MHD growth-rates of the internal kink. It therefore appears plausible that diamagnetic rotation can stabilize the internal kink as long as its resistive-MHD growth-rate is not too large.

By comparing Figs. 2a-c for different values of S, we note a gradual change in the main factor determining the growth-rate. At $S = 10^6$, the growth-rates are mainly dependent on q_p, i.e., on the shear at the q = 1 surface, and are only weakly dependent on the pressure. This is typical of the resistive kink mode. This picture is modified somewhat at $S = 10^8$ which represents an intermediate case. The three lower curves in Fig. 2b ($\beta_{pol} = 0.00, 0.05, 0.10$) still show reasonably high growth-rates (about $2 \times 10^{-3}\ \omega_A$) for a current driven resistive mode, but for $\beta_{pol} \leq 0.1$, the pressure has only a weak influence on the growth-rates. For $\beta_{pol} = 0.15$, destabilization by pressure becomes significant. An interesting aspect of this "pressure driven" instability is that it is clearly sensitive to the q-profile and its growth-rate rises sharply when the q = 1 surface moves out into the region of high shear. Thus, although the instability is *pressure driven*, it can be thought of as being *triggered* by the *current profile*.

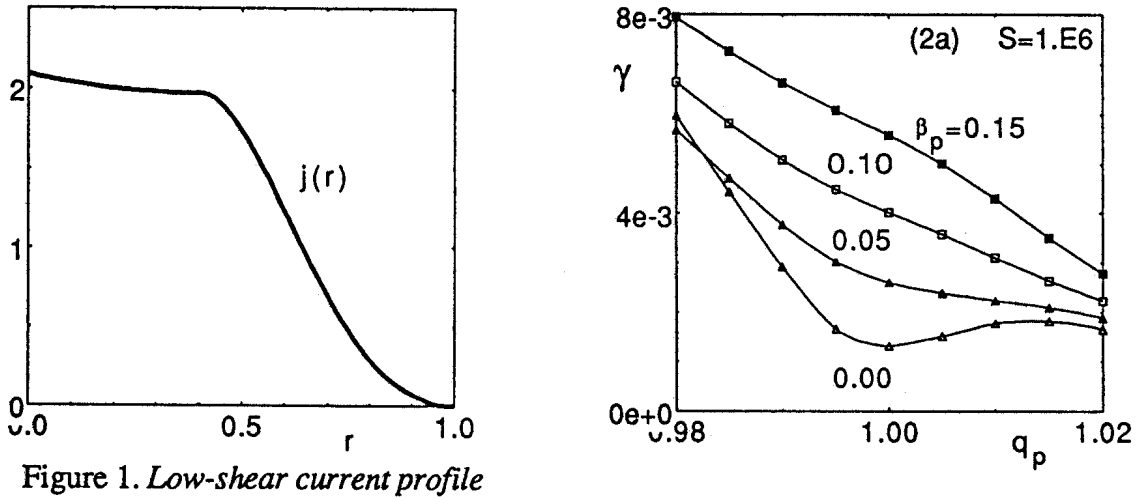

Figure 1. *Low-shear current profile*

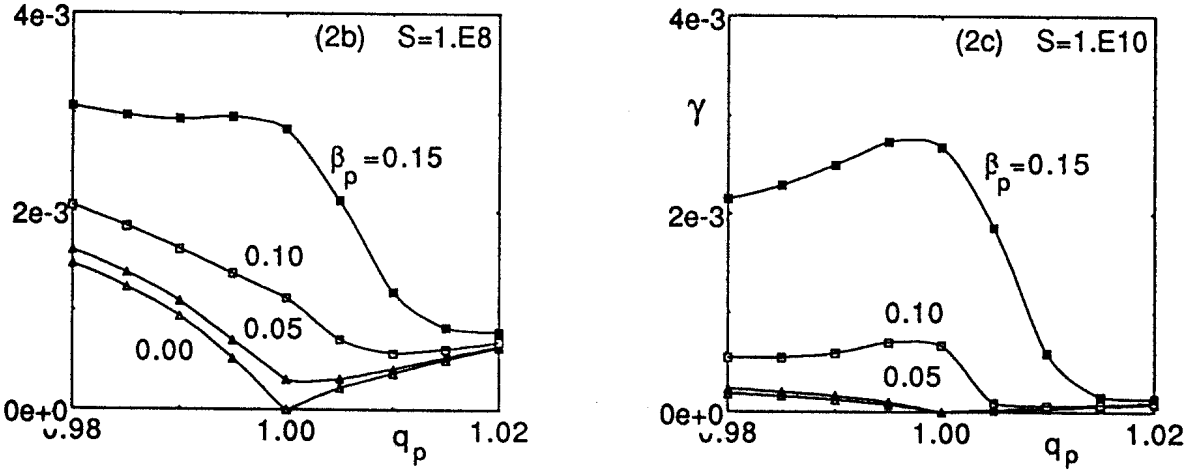

Figure 2. *Resistive growth-rates for low-shear current profile and different β_{pol}*

Much more clear changes from the low-S picture are seen in Fig 2c for $S = 10^{10}$. Here, the resistive growth-rates for $\beta_{pol} = 0.00$, and 0.05 are rather small (a few times $10^{-4}\ \omega_A$) and the pressure driven instability is clearly dominant. Comparing the growth-rates with those for $S = 10^8$, we see that the pressure driven instability is essentially ideal. Thus, it appears that as S is increased, the linear instability leading to the sawtooth crash becomes more and more an ideal, pressure driven instability. However, *this ideal mode is sensitive to details of the current profile and can be triggered by a slight shift in the q-profile.* In fact, the variation of the

growth-rate with q_p at high S and not-too-small β_{pol} is more pronounced than for the resistive kink mode at low S. Figure 2c also shows that the critical β_{pol} for ideal stability is rather low, about 0.1 for this current profile. We have obtained results similar to those in Fig. 2 for a current profile with twice the shear in the central region. In this case, the resistive mode at low pressure gives somewhat higher growth-rates than the low-shear case shown in Fig. 2.

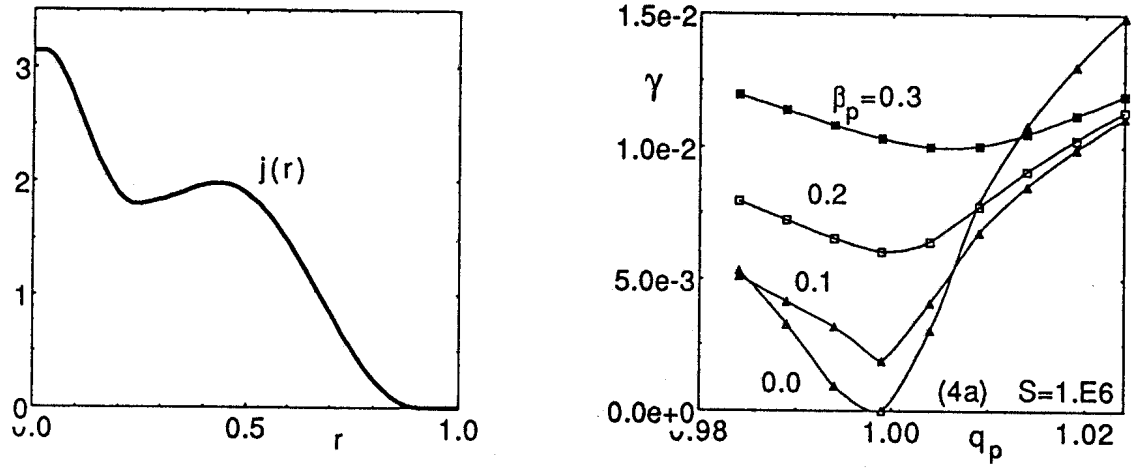

Figure 3. *TEXTOR current profile*

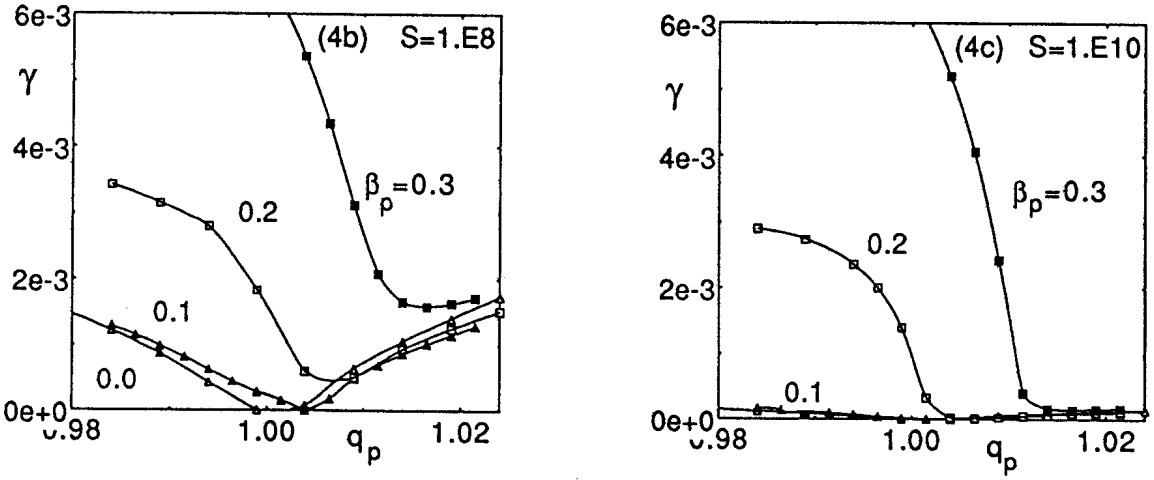

Figure 4. *Resistive growth-rates for TEXTOR current profile and different β_{pol}*

We have also computed resistive growth-rates for a current profile of TEXTOR type, as shown in Fig. 3. The shoulders in the current profile were adjusted so that the shear has a minimum of about 0.034 at $r = r_p \approx 0.44a$. In this case, the global shear in the central region is strong and $q_0 \approx 0.634 q_p$ is well below unity. Figure 4 shows the growth-rates for different S-values and $\beta_{pol} = 0.0$, 0.1, 0.2, and 0.3. In general terms, the behavior is similar to that for the low-shear profile, but the TEXTOR profile supports about twice the pressure before becoming ideally unstable.

III. WALL AND SHAPING EFFECTS

Although the displacement of the internal kink mode is mainly localized to the region inside the q = 1 surface, the magnetic perturbation outside q = 1 is not small and it is important for the mode stability [5]. Numerically, we find that the ideal stability boundaries are strongly influenced by wall position when the q = 1 radius is sufficiently large and the aspect ratio is low. As an example, Fig. 5a shows growth-rates for the ideal internal kink as a functions of β_{pol} at q=1 for a sequence of circular equilibria with $r_{q=1}/a \approx 0.6$ and edge q between 2 and 3. Two different wall positions have been considered: b/a = 1 (fix boundary) and b/a = 2 (free boundary). For this equilibrium, we find that the difference in marginal β_{pol} between the fix and free boundary cases scales as the square of the inverse aspect ratio, as expected from large aspect ratio theory. At low aspect ratio, the wall position plays a significant role; the marginal β for free boundary stability is only about half of the fixed boundary value for R/a = 2.7. When the edge q is raised above 3 for the circular equilibrium, the influence of the wall position is weak and not of practical significance.

In the case of shaped cross-section and a large q = 1 surface, the wall position has a more dramatic influence. An example is shown in Fig. 5b for JET-shaped cross-section with elongation κ = 1.7 and triangularity δ = 0.3. The aspect ratios are A = 3.5, 6, and 10, respectively, and $r_{q=1}$ = 0.6a and q_0 = 0.7 are held fixed. The edge q varies with aspect ratio but remains between 3 and 4. For this equilibrium, the wall has a strong influence independent of the aspect ratio. Note that for A > 4.5, the equilibrium is free-boundary unstable even at zero beta. This, too, is in agreement with large aspect ratio theory, as δW contains stabilizing terms $\propto (r_{q=1}/R)^2$ and destabilizing terms $\propto (\kappa-1)^2$. Thus, at fixed κ > 1, large aspect ratio theory predicts instability even at zero beta when the aspect ratio is sufficiently large. Triangularity has a stabilizing influence, but for JET geometry and the q-profile used here, this stabilization is insufficient to compensate for the destabilization by ellipticity.

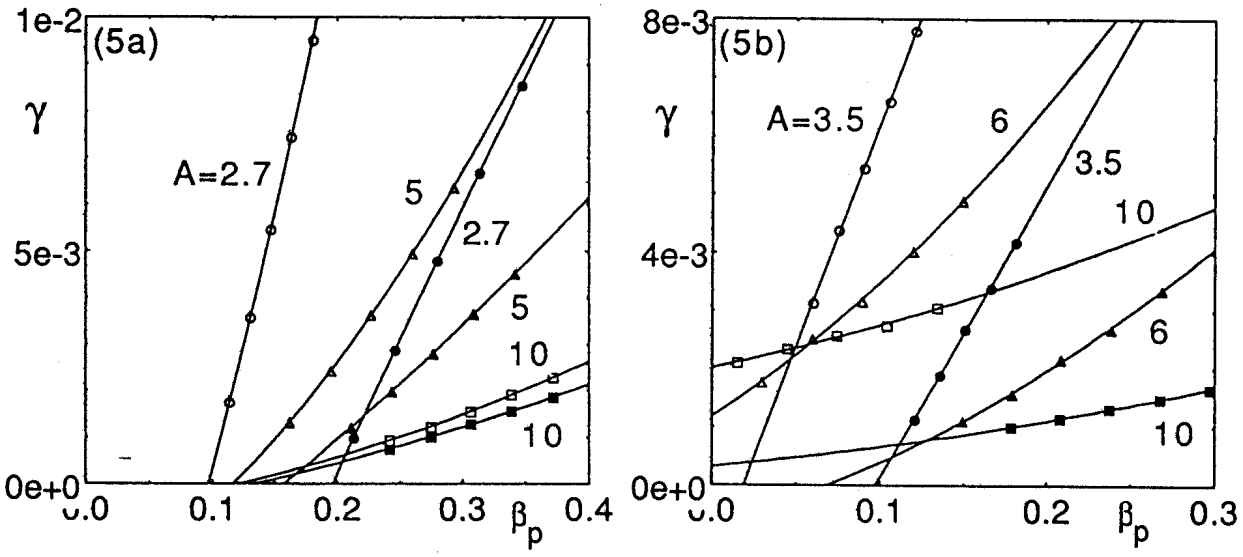

Figure 5. *Ideal growth-rates for free and fixed boundary at different aspect ratios. Free boundary is indicated by open symbols. (a) Circular and (b) JET cross-section*

REFERENCES

1. H. Soltwish, W. Stodiek, J. Manickam, *et al*, IAEA Kyoto (1986), Vol I, p. 263.
2. A. Bondeson, G. Vlad and H. Lütjens, EPS Amsterdam (1990), Vol. II, p.906.
3. H. Lütjens, A. Bondeson, and A. Roy, LRP 405/90, submitted to Comput. Phys. Comm.
4. W. Park and D.A. Monticello, Nucl. Fusion **30**, 2413 (1990).
5. M.N. Bussac, R. Pellat, D. Edery and J.L. Soule, Phys. Rev. Lett. **35**, 1638 (1975).